Geophysical characterisation of active thermogenic oil seeps in the salt province of the lower Congo basin part I: Detailed study of one oil-seeping site

Romain Jatiault, Lies Loncke, Damien Dhont, Patrice Imbert, Dominique Dubucq

Geophysical characterisation of active thermogenic oil seeps in the salt province of the Lower Congo Basin Part I: detailed study of one oil-seeping site

Romain Jatiault [a, b]*, Lies Loncke [b], Damien Dhont [a], Patrice Imbert [a], Dominique Dubucq [a]

[a] Total SA, Centre Scientifique et Technique Jean Feger (CSTJF), Avenue Larribau, 64018 Pau, France

[b] University of Perpignan Via Domitia, Centre de Formation et de Recherche sur les Environnements Méditerranéens (CEFREM), UMR 5110, 52 Avenue Paul Alduy, 66100 Perpignan, France

*Corresponding author. University of Perpignan Via Domitia, Centre de Formation et de Recherche sur les Environnements Méditerranéens (CEFREM), UMR 5110, 52 Avenue Paul Alduy, 66100 Perpignan, France. Tel.: +334 68 66 20 98

E-mail addresses: romain.jatiault@univ-perp.fr, romain.jatiault@gmail.com (R. Jatiault)

Abstract

We report the geophysical characterisation of natural oil seep sites through a combination of sea surface evidence of oil leakage from spatial imagery with a large collection of seafloor and subsurface geophysical data. This paper provides a detailed characterization of one selected active seep site and identifies possible specific feature of oil seep sites. The oil seep is a complex-shaped feature on the seafloor consisting of a cluster of heterometric pockmarks inside a main depression area and peripheral metre-scale seafloor mounds. A strong deformation related to salt tectonics controls the location of the seafloor source by fracturing the overburden. The associated thermal anomaly induces a vertical modification position of the base of the gas hydrate stability zone (BGHSZ) that is used as a fluid migration route towards the crest of the diapir. The combination of local depressions and seafloor amplitude anomalies linked with vertical high-amplitude pipes rooted on the BGHSZ suggests a focused fluid flow towards the seafloor. In peripheral areas, the seafloor mounds are linked by shallow faults to buried high amplitude patches on sub-bottom profiler sections. The combination of restricted-size seafloor mounds with a progressive deepening of the high amplitude from the seafloor suggests a substantial decrease of the hydrocarbon flow towards peripheral areas. The proximity of actively oil-supplying seafloor depressions and seafloor mounds shows that the hydrocarbon flow rapidly decreases laterally. The thermogenic seep site is affected by two consistent and sub-parallel reflections with negative polarity. The first is interpreted as the methane-related BGHSZ, the second could correspond to the base of a thermogenic BGHSZ produced by a mixture of heavier gas. The seafloor roughness and double BSR appear to be specific features of oil seep sites. The geophysical features revealed at a localised study area will be extrapolated towards a larger province for relevance validation.

34 # Keywords

35 ***Oil slicks; Thermogenic seeps; Pockmarks; Asphalt; Salt diapir; Lower Congo Basin; Gas hydrates;***

36 ***Double BSR***

37 # Abbreviations

AOM	Anaerobic Oxydation of Methane	NAA	Negative Amplitude Anomaly
AUV	Autonomous Underwater Vehicle	OSO	Oil Slick Origins
BGHSZ	Base of the Gas Hydrate Stability Zone	RMS	Root Mean Square
BSR	Bottom Simulating Reflection	SAR	Synthetic Aperture Radar
ERS	European Remote Sensing	SBP	Sub-Bottom Profiler
GMC	Geometric Mean Centre	SMI	Sulphate Methane Interface
HAB	High Amplitude Bodies	TOC	Total organic Carbon
HIL	High Impedance Layer	TWT	Two Way Time
IMP	Image Mode Precision	WSM	Wide Swath Mode
LCB	Lower Congo Basin		

38

1. Introduction

The study of natural fluid escape has both industrial and academic implications. Natural hydrocarbon seeps are widely used by petroleum companies as an exploration tool as they provide evidence for an active petroleum system (***Abrams, 2005; Serié et al., 2016***). The evaluation of active seeps also bears implications in terms of deep-sea geohazards as it enhances the risk of slope failure (***Acosta et al, 2005; Bünz et al., 2005; Judd and Hovland, 2009; Gwiazda et al., 2016***). For environmental purposes, the recognition of hydrocarbon seeps helps to identify habitats for extreme environment ecosystems (***Ondreas et al., 2005; Judd and Hovland, 2009; Jones et al., 2014***) and to locate potential hydrocarbon input into the hydro/atmosphere (***Wilson et al., 1973; Kvenvolden and Harbaugh, 1983; Kvenvolden and Cooper, 2003; National Research Council, 2003; Etiope et al., 2015).***

The seafloor morphological expression of fluid seepage occur as mud volcanoes, mounds or pockmarks, defined as depressions associated with active focused fluid flow (***King and MacLean, 1970; Hovland, 1981; Hovland and Judd, 1988; Judd and Hovland, 2009; Hovland et al, 2010; Andresen and Huuse, 2011; Andresen, 2012***). Pockmark geometries range from circular to elliptical (***Hovland, 1981; Hovland et al., 1984; Hovland et al., 2010; Andresen and Huuse, 2011; Andresen, 2012***). The depression diameters range from less than 5 m (***Hovland et al., 2010***) up to over 1 km, as in the Regab pockmark in offshore Gabon (***Charlou et al., 2004; Ondreas et al., 2005; Gay et al., 2006c; Marcon et al., 2014***). The vertical migration of hydrocarbons through sedimentary series is typically expressed as clustered pipes or large-scale isolated chimneys identified as vertical columns of acoustic disturbance on geophysical sections (***Loncke et al., 2004; Gay et al., 2006a, b; Dupré et al., 2007; Moss and Cartwright, 2010, Løseth et al., 2011, Karstens and Berndt, 2015***). Both biogenic (action of bacteria at shallow depths) and thermocatalytic processes (effect of heat and pressure during the burial of sediments; ***Floodgate and Judd, 1992; Stolper et al., 2015***) are known to

63 generate hydrocarbons. However, geophysical subsurface imagery is unable to characterise the fluid
64 type and to discriminate biogenic gas from heavier thermogenic seepage. Seafloor coring provides a
65 precise means to evaluate the nature of hydrocarbons on the seafloor (***Abrams, 2005***) but requires
66 the deployment of relatively heavy toolsets. Recurrent oil seepage slicks at the sea surface are
67 detectable with space-borne Synthetic Aperture Radar (SAR) tools (e.g. ***Gade and Alpers, 1998;***
68 ***Espedal and Johannessen, 2000; Hood et al., 2002; MacDonald et al., 2002; Williams and Lawrence,***
69 ***2002; Brekke and Solberg, 2005; Zatyagalova et al., 2007; Garcia-Pineda et al., 2010; Körber et al,***
70 ***2014; Jatiault et al., 2017***); identifying their presence attests to active thermogenic migration and
71 ultimately helps to locate active oil seeps at the seabed (***Macdonald et al., 1993; de Beukaleaur et***
72 ***al., 2003; Garcia-Pineda et al., 2010; Körber et al., 2014; Serié et al., 2016; Jatiault et al., 2017***). The
73 integration of SAR imagery, seismic datasets and geochemical analyses have demonstrated their
74 efficiency to understand hydrocarbon plumbing systems (***Garcia-Pineda et al., 2010; Serié et al.,***
75 ***2016***).

76 In contrast with the well-documented gas systems, the detailed description of seafloor features
77 associated with oil seep systems is restricted to a few case studies, mostly the Santa Barbara Basin
78 (***Keller et al., 2007; Valentine et al., 2010***), the Gulf of Mexico (***MacDonald et al., 2004; Sahling et***
79 ***al., 2016***) and the Lower Congo Basin (***Unterseh, 2013; Jones et al., 2014***). The prediction of oil-
80 supplying pockmark characteristics has strong implications for petroleum exploration decisions and
81 on the selection of coring targets. We investigated the possible specificity of the geophysical
82 signature of oil compared to gas by studying fluid migration features of oil-dominated seep sites.

83 The aim of this paper is first to assess the geophysical characteristics of oil seeps both on the seafloor
84 and in the subsurface to understand whether specific attributes can be associated with active oil
85 seep sites and then to offer an integrated high-resolution description of one thermogenic seep in the
86 Lower Congo Basin. We will approach the oil seeps on the seafloor by combining different resolution

datasets of subsurface seismic imagery used for petroleum exploration together with space-borne SAR imagery.

2. The study area

2.1 Geological setting

The Lower Congo Basin (LCB) is located in the northernmost offshore part of the Angolan margin (Fig. 1 a). The LCB extends over 115,000 km² (***Da Costa et al., 2000***) and is delimited to the north by the Gabon basin, to the south by the Ambriz arch (***Davison, 1999; Moulin et al., 2005; Guiraud et al., 2010; Moulin et al., 2010***; Fig. 1 Fig. 1a). It results from the break-up of Gondwana into the South American and African plates initiated in the Early Cretaceous (e.g. ***Lehner and de Ruiter, 1977; Brice et al., 1982, Duval et al., 1991; Marton et al., 2000; Marton et al., 2004; Beglinger et al., 2012***). The deposition of a thick (up to 1000 m) evaporite layer (Loëme salt; Late Barremian to Aptian), mostly composed of massive halite topped by anhydrite (***Brice et al., 1982; Teisserenc and Villemin, 1989; Uchupi, 1992; Karner et al., 1997; Da Costa et al., 2000; Marton et al., 2000; Anka et al., 2009; Andresen and Huuse, 2011***) occurred after the end of the rifting phase. The hydrocarbon source rocks are the pre-salt lower Cretaceous **Bucomazi Fm** (***Burwood, 1999; Cole et al., 2000***) and the post-salt upper Cretaceous **Iabe Fm**, (***Cole et al., 2000; Schoelköpf and Patterson, 2000; Séranne and Anka, 2005***). Tertiary deposits dominantly consist of mudstones and shales alternating with sand-rich turbidite channel/levee deposits. The **Landana Fm** (65 - 45 Ma; ***Cole et al., 2000, Schoelköpf and Patterson, 2000*** and **Malembo Fm (35 - 5Ma)** include high potential source rock formations, but these are mostly immature through the LCB due to insufficient burial (***Cole et al., 2000***). The shift of the paleo Congo River to its present-day location at the Miocene-Pliocene boundary (***Ferry et al., 2004; Savoye et al., 2009***), coupled with upwelling that enhanced primary productivity during the Early Quaternary modified sedimentation type towards fine deposits above the abandoned Miocene deep sea fan (***Jansen, 1985; Uenzelmann-Neben, 1998)***. The post-salt sedimentary overburden is

111 highly deformed and translated towards the basin by salt tectonics where evaporites act as a
112 decollement layer. As a result, the basin is subdivided into three main structural domains as follows,
113 from proximal to distal (Fig. 1 a, b). The proximal extensional domain are mostly constitutes in the
114 deposits of the Neogene Congo delta (***Séranne and Anka, 2005***). Strong extensional deformation,
115 dominated by rafts and grabens, evidenced by normal faulting and salt rollovers results in a
116 widespread distribution of rafts and grabens that now corresponds to sealed blocks in the area (***Brice***
117 ***et al., 1982)***. Evaporite series are restricted to thin residual deposits along the basal detachment,
118 along with occasional salt pillows, in relation to the basinward translation of the overburden (***Brice et***
119 ***al., 1982; MacHargue, 1990; Duval et al., 1991; Burwood, 1999; Schoellkopf and Patterson, 2000***).
120 The transitional/translated domain is characterised by isolated salt diapirs that pierce through the
121 seaward-translated post-salt series. The distal compressive domain is characterised by intense
122 folding and salt thickening. Gravity-driven translation of the Tertiary sedimentary cover led to a
123 drastic compression in the distal areas which expresses as a large diversity of salt bodies such as
124 domes, shallow walls or nappes (for an overview of allochthonous salt types, see ***Warren, 2016***).
125 Basinward compression together with ongoing salt tectonics led to the formation of squeezed diapirs
126 (***Brun and Fort, 2004; Fort et al., 2004***). Ongoing salt tectonics concentrated the deposits of the post-
127 rift super-sequence into minibasins that are characterised by confined channel/levee systems and
128 turbidite fans (***Oluboyo et al., 2014***).

129 The study area is affected by a prolific fluid seepage system as described in literature (***Lucazeau et***
130 ***al., 2004; Gay et al., 2006b,c; Gay et al., 2007; Andresen et al., 2011; Andresen and Huuse, 2011;***
131 ***Andresen, 2012; Imbert and Ho, 2012; Anka et al., 2013; Jones et al., 2014; Wenau et al., 2014 a,b;***
132 ***Maia et al., 2016; Jatiault et al., 2017; Jatiault et al., 2018***), mostly constrained in the downslope
133 compressive province. Two types of pockmarks on the seafloor were described in the area; (1) bulls-
134 eye pockmarks described by ***Andresen et al. (2011)*** and defined as a vertical succession of stacked

sub-circular depressions located in the centre of polygonal fault cells; (2) Clustered pockmarks consist of a complex aggregation of various size pockmarks (***Andresen, 2012***).

2.2. Study area selection

We focus this paper on one isolated oil seep site to perform a local and detailed study of the seafloor/sub-seafloor features associated with one selected thermogenic seep sites in the LCB based on data coverage. We investigated a zone of the Lower Congo Basin where a large amount of expelled oil was recognised regionally at the sea surface (***Williams and Lawrence, 2002; Jatiault et al., 2017***). The first criterion of selection refers to the availability of seafloor and subsurface geophysical data, which consists of 3D exploration seismics and 2D, high-resolution geohazard survey data. A large number of recurrent oil seep sites (102) reported in this province (***Jatiault et al., 2017***) are imaged by the 3D seismic cube but only 7 high-confidence oil seep sites are imaged with both the 2D, HR geohazard survey and 3D seismics. The amount of available SAR scenes were also considered for the site selection (***MacDonald et al., 1996; Garcia-Pineda et al., 2010; Korber et al., 2014***). The seep site investigated in this paper benefits from a high SAR coverage density (136 overlapping SAR scenes) and revealed frequent oil emission phases (high ratio between detected slicks and SAR data coverage). The selected sites in this study is located at the limit between the translated and compressive domain, where the water depth is about 1650 m (Fig. 1).

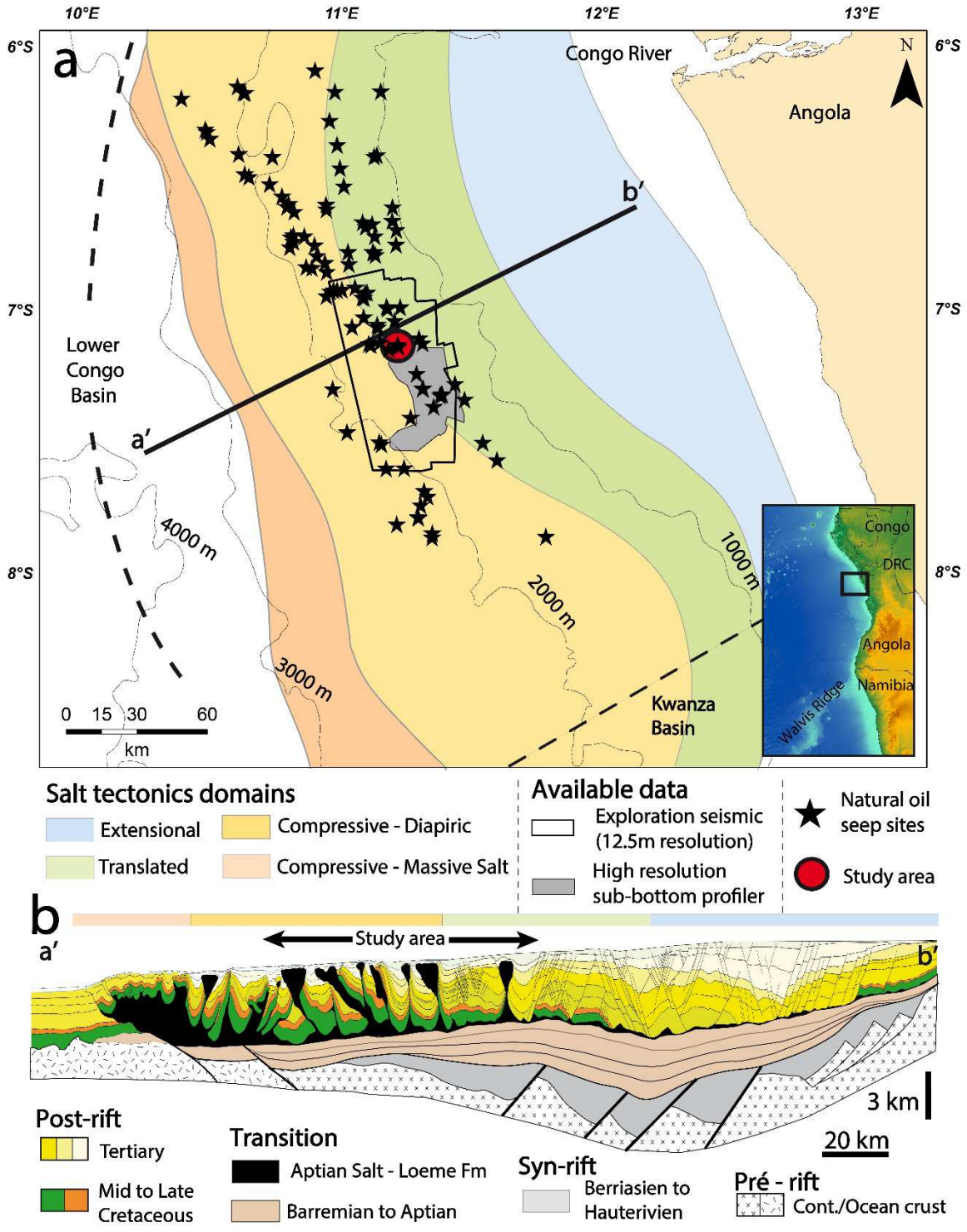

152

153 **Fig. 1: a. Location map of the study area showing the main geological provinces of the LCB. Black**

154 **stars correspond to recurrent oil slicks at the sea surface (Jatiault et al., 2017). Continuous black**

lines represent 1000 m isobaths (Gebco - https://www.gebco.net). b. Regional cross section across the LCB displaying the pre-rift, syn-rift and post-rift sequences (modified from Jatiault et al., 2017).

3. Material and methods

3.1 Sea surface mapping of natural oil slicks

The SAR system is sensitive to capillary waves induced by the local wind at the sea surface (e.g. ***Franceschetti et al., 2002; McCandless and Jackson, 2003***). We used published mapping of natural seepage slicks at the sea surface in the LCB interpreted from 104 SAR scenes (***Jatiault et al., 2017***), which we complemented with 52 Cosmo-Skymed scenes delivered every 15 days during 2013 and 2014 together with Sentinel-1 data acquired between 2015 and 2016. The delineation of elongated seepage slicks is based on the analysis of radiometric anomalies associated with oil-covered areas (***MacDonald et al., 1993; Espedal and Johannessen, 2000; Johannessen et al., 2000; MacDonald et al., 2002; Alpers and Espedal, 2004; Brekke and Solberg, 2005; Garcia-Pineda et al., 2009; Fingas and Brown, 2014***).

Diverging structures on the stack of slick outlines highlights recurrent oil seeps due to current variability at the sea surface; their centre pinpoints the locations of active oil seeps (***Kornacki et al., 1994; MacDonald et al., 1996; de Beukelear et al., 2003; Zatyagalova et al., 2007; Garcia-Pineda et al., 2010; Garcia-Pineda et al., 2014; Körber et al., 2014; Jatiault et al., 2017***). We draw visually the Oil Slick Origins (OSO, ***Garcia-Pineda et al., 2010; Körber et al, 2014***) from the location of the proximal detectable edge of each oil slick. Posting all the OSO on a map highlights clusters of points whose spatial dispersion results from the horizontal deflection of the oil plume when rising through the water column; the minimum-size circles encompassing each single OSO expelled from individual seep sites then help to evaluate the offset range values generated by underwater deflection (***Garcia-Pineda et al., 2010; Jatiault et al., 2018***). In areas where hydrodynamic conditions are not affected by a dominant current, the vertical projection of the OSO density coupled with the location of the

OSO barycentre (Geometric Mean Centre: GMC; ***Garcia-Pineda et al., 2010***), at the sea surface provides an additional means to estimate the location of the active seep on the seafloor (***Körber et al., 2014; Jatiault et al., 2018***). Multiple slick patterns are commonly observed on SAR scenes (***Garcia-Pineda et al., 2010; Jatiault et al., 2017).*** The low residence period of oil slicks (a few hours; ***Jatiault et al., 2017***) suggests that multiple slicks with identical patterns (same geometry, same orientation) likely reflect concomitant emission from distinct sources rather than oil slicks relics expelled during former active stages. To link sea surface manifestations with seafloor features, we used the fact that OSO are mostly constrained within restricted-size circles of 2500 m radius with an average distance between individual OSO and the GMC of roughly 750 m. This shows that the spatial dispersion of individual OSO over time remains low compared to the water depth (1100 - 2700 m), eventually due to reverse currents that decrease the deflection outcome (***Jatiault et al., 2018)***

3.2. Seafloor and sub-seafloor geophysical dataset

The geophysical dataset used in this study is composed of a 3D seismic cube, sub-bottom profiler (SBP) sections and high-resolution multibeam seafloor imagery acquired with an Autonomous Underwater Vehicle (AUV). The characteristics of the geophysical data of both seafloor and sub-seafloor imagery are displayed in table 1.

Table 1: Characteristics of the available datasets including seafloor and sub-seafloor imagery.

Data type		Line spacing (m)	Maximum Penetration (ms TWT)	Dominant frequency	Horizontal Resolution (m)	Vertical Resolution (m)	Spatial coverage/ Total length of acquisition
Sub-seafloor	3D seismics	12.5 * 12.5	4500	~20 - 100 Hz	12.5	~ 4 m	3300 km²
	Sub-Bottom Profiler	175 * 1000	100	1.5 - 4.5 kHz	1.5	~ 10 cm	1515 km
Seafloor	AUV HR bathymetry	-	-	200 kHz	3	-	220 km²
	AUV Seafloor Reflectivity	175 *	Several centimetre	120-410 kHz	3	-	220 km²

		1000	**s**				

3.2.1. 3D exploration seismics

The 3D seismic volume covers 3300 km² (Fig. 1a) with a record length of 4500 ms TWT. The acquisition source consists of 2 Texas Instrument sleeve airguns clusters (8 guns per source), 50 m apart with shot point intervals of 25 m at a depth of 5m. The source volume is 2*3000 cubic inches, operating a pressure of 2000 psi. The acquisition system consists of 10 parallel Thomson Marconi Sonar Sentry streamers separated by 100 m. Each streamer is composed of 396 individual receiver groups separated by 25 m (total length of 4950 m). The seismic cube used in this study is Pre-Stack Time Migration (PSTM). The seismic processing sequence (PGS Viper processing sequence) consisted first in time-migration and normal move-out correction using auto-picked velocities every 2000m and followed by the stacking of seismic traces. The distance between adjacent seismic lines is 12.5m following a nominal geometry derived from the navigation data. A 2 Hz low-cut and a 206 Hz high-cut filters were applied. A 3dB/sec display gain was used between 0 to 4500 ms. We carried out interpretation on the near-offset seismic cube. Seismic sections in the figures display the amplitude of the reflected signal. The colorscale is centred on zero, positive amplitude values indicating a downward increase of impedance at lithologic interfaces are displayed in warm colours. Negative impedance contrasts are displayed on a grey scale. The seismic amplitudes were extracted using the chaotism seismic attribute based on a semblance criterion across a window and computed with the Root Mean Square (RMS) seismic amplitude (***Andresen et al., 2011***).

3.2.2. High-resolution geophysical survey

The high-resolution SBP 2D lines (Edgetech DW-216 Chirp profiler system) were acquired for site surveys and geo-hazards evaluation with an AUV, following a regular grid with a line spacing of 1000 m in the alongslope direction and 175 m in the cross-slope direction. The high-frequency data enable good vertical resolution (~10 cm) but with an acoustic wave penetration limited to the first 100 ms TWT below the seafloor (Table 1). The picking of horizons on the SBP sections was performed using

220 the amplitude attribute; for visibility purposes, due to the very high frequency of the signal, sections
221 are displayed on the figures with the envelope filter that averages the signal (RMS) over a sliding
222 window.

223 In addition to the SBP sections, the AUV device is equipped with a high-resolution (HR) multibeam
224 echo-sounder (EM2000 Simrad; 200 kHz) and a side-scan sonar device recording seafloor reflectivity
225 (Edgetech Full Spectrum Chirp dual frequency DW-120/410 side scan sonar system) along the
226 acquisition tracklines of the vehicle. The survey covers an area of 220 km² with a spatial resolution of
227 3 m. Seafloor imagery also provides seafloor backscatter that can be used as a proxy for seafloor
228 hardness evaluations. The surveyed area (220 km²) remains larger than the area investigated in this
229 study. Overlying the gradient with the seabed isochron enhances the imagery of seafloor features.
230 The architecture of the salt-related deformation is assessed from the interpretation of the 3D
231 seismics because the line spacing between SBP sections is insufficient to ensure reliable correlation
232 between faults picked on adjacent lines.

233

4. Analysis and results

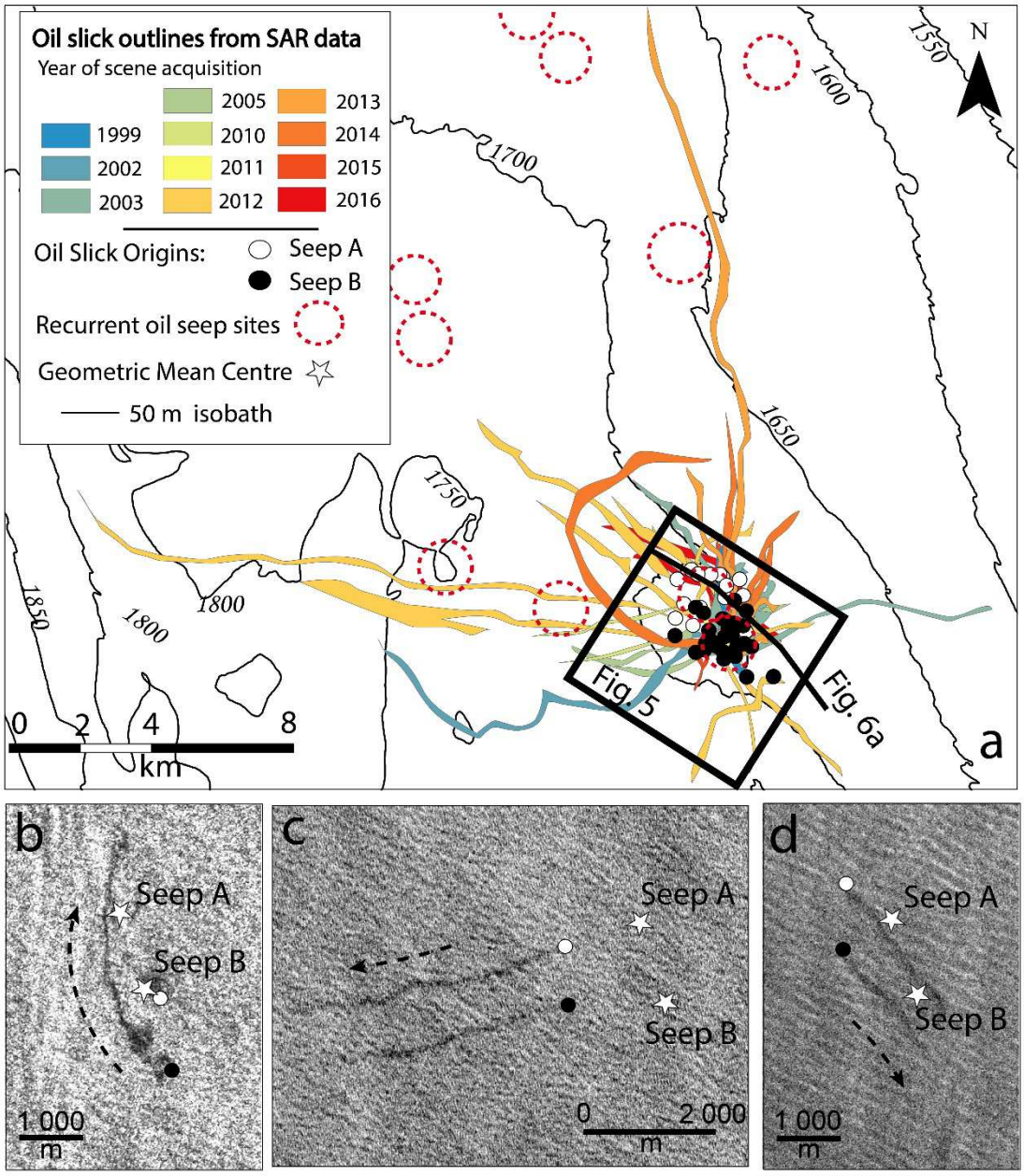

Fig. 2: a. Compilation map of seepage slicks identified in the chosen study area from the analysis of the 136 overlapping SAR scenes. The colour scale refers to the year of slicks related to the SAR acquisition period. White and black dots are the OSO locations for seep sites A and B respectively. The slick outlines identified at the sea surface are superimposed with 50 m seafloor isobaths. Recurrent oil seep sites are encircled with red dashed circles. b. Extract of Envisat IMP scene dated

12/02/1999. c. Extract of Cosmo-Skymed SAR scene dated 22/11/2010. d. Extract of Cosmo-Skymed SAR scene dated 10/01/2011. White stars correspond to the GMC locations in insets b,c,d.

4.1 Sea surface evidence of natural oil seepage

Sea surface manifestations of oil leakages were observed between 1999 and 2016 but most seepage slicks were identified after 2010 due to an increase in SAR data acquisition (Table 2). A total of 44 slicks were identified as diverging from the oil seeping zone investigated in this study based on the analysis of the 136 overlapping scenes. The slick geometry occurred as curvilinear, straight or zigzagging shapes (Fig. 2), radially deflected from the central surfacing area. The slick width remained constant along the slick shape from the proximal OSO towards the distal edge as seen on successive SAR scenes. The length of seepage slicks ranged from 2 to 18 km and the surface area of individual seepage slicks ranged from 0.12 to 3.2 km² with an average value of 0.7 km² (Table 2). Distinct twin slicks were frequently identified (20 slicks out of the 44 mapped) and interpreted as expelled from two distinct oil seep sites, 1250 m apart (Seep A and Seep B in Fig. 2). For seep A and B respectively, the occurrence rate ratios compared to the SAR scene coverage were 11% (16/136) and 21% (28/136) and the OSO gathered within circles of radii of 1200 and 1500 m (Fig. 3a). The maximum OSO density occurred at the location of the GMC of seep B and remained high within a radius roughly 750 m from the GMC of seep A and B (red to green in Fig. 3a) and rapidly decreased outwards. The maximum observed horizontal deflection value from GMC to individual OSO was 1750 m.

260 **Table 2: Seepage slicks overview identified on spaceborne SAR scenes and released from the oil seep areas investigated in this study.**

Date (dd/mm/yyyy)	Sensor	Seep	Area (km^2)	Distance from OSO to GMC (m)	Date (dd/mm/yyyy)	Sensor	Seep	Area (km^2)	Distance from OSO to GMC (m)
12/02/1999	ERS/IMP	A	**0.34**	**1420**	**27/03/2012**	Cosmo-SkyMed	A	**0.26**	**570**
12/02/1999	ERS/IMP	B	**0.4**	**1270**	**06/04/2012**	Envisat/WSM	A	**2.35**	**1200**
07/12/2002	Envisat/WSM	A	**2.4**	**910**	**06/04/2012**	Envisat/WSM	B	**3.17**	**950**
14/01/2003	Envisat/WSM	B	**0.7**	**570**	**13/10/2012**	TerraSAR-X	B	**0.22**	**450**
06/03/2003	Envisat/WSM	B	**0.6**	**410**	**17/10/2012**	Cosmo-SkyMed	B	**0.21**	**450**
14/03/2003	Radarsat	B	**0.89**	**610**	**21/10/2012**	TerraSAR-X	B	**0.25**	**610**
28/03/2003	ERS/IMP	A	**0.68**	**510**	**21/10/2012**	Cosmo-SkyMed	B	**0.69**	**190**
25/11/2003	Envisat/WSM	B	**0.22**	**420**	**27/05/2013**	Cosmo-SkyMed	B	**2.83**	**190**
19/02/2005	Envisat/WSM	B	**0.24**	**780**	**16/07/2013**	Cosmo-SkyMed	B	**0.52**	**1050**
22/02/2005	Envisat/WSM	A	**0.56**	**1000**	**23/12/2013**	Cosmo-SkyMed	A	**0.27**	**940**
22/02/2005	Envisat/WSM	B	**0.41**	**700**	**23/12/2013**	Cosmo-SkyMed	B	**0.21**	**360**
22/11/2010	Cosmo-SkyMed	A	**0.29**	**820**	**19/02/2014**	Cosmo-SkyMed	B	**0.55**	**430**
22/11/2010	Cosmo-SkyMed	B	**0.2**	**1430**	**20/05/2014**	Cosmo-SkyMed	B	**1.07**	**320**
10/01/2011	Cosmo-SkyMed	A	**0.24**	**700**	**28/07/2014**	Cosmo-SkyMed	B	**0.61**	**940**
10/01/2011	Cosmo-SkyMed	B	**0.22**	**1190**	**16/09/2014**	Cosmo-SkyMed	B	**2.76**	**580**
26/01/2012	Envisat/WSM	A	**0.57**	**910**	**11/11/2015**	Sentinel-1a	A	**0.18**	**390**
06/02/2012	Envisat/WSM	A	**1.49**	**1050**	**11/11/2015**	Sentinel-1a	B	**0.14**	**510**
06/02/2012	Envisat/WSM	B	**0.96**	**910**	**05/12/2015**	Sentinel-1a	A	**0.27**	**620**
14/02/2012	Envisat/WSM	B	**0.32**	**510**	**05/12/2015**	Sentinel-1a	B	**0.12**	**30**
15/03/2012	Envisat/WSM	B	**0.13**	**590**	**15/04/2016**	Sentinel-1a	A	**0.23**	**600**
18/03/2012	Envisat/WSM	B	**0.74**	**1760**	**08/07/2016**	Sentinel-1a	A	**1.04**	**900**
26/03/2012	Envisat/WSM	A	**0.41**	**470**	**08/07/2016**	Sentinel-1a	B	**0.68**	**440**

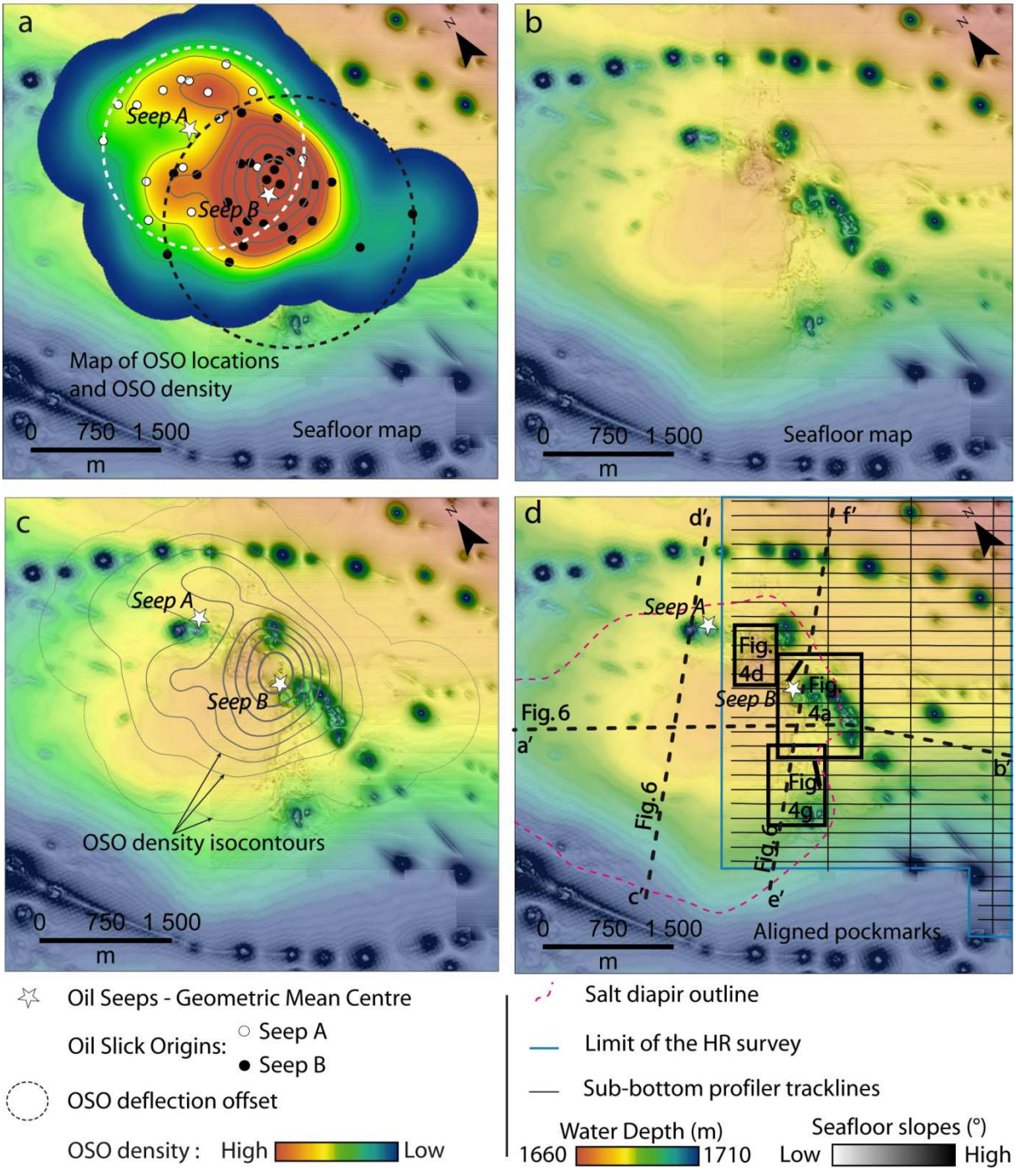

261

262 **Fig. 3: a. Location of individual OSO and bounding circles of the deflection offset. White stars show**
263 **the location of the GMC for seep A and seep B. Individual OSO locations are superimposed with the**
264 **density map of OSO. Deep red to greenish colours refer to high OSO density. b. Bathymetric map**
265 **composed of 3D seismics first arrivals and available high-resolution bathymetry where available,**
266 **superimposed with slope map. c. Bathymetric map superimposed with OSO isocontours.**

Concentric circles show the increase in density of OSO. d. Bathymetric map superimposed with SBP tracklines. Pink dotted line corresponds to the underlying salt diapir extension.

4.2. Seafloor geophysical features associated with the oil seep site

Oil slicks diverge from a large depression located above the edge of the underlying diapir (pink dotted line in Fig. 3d). The morphology of the seafloor below the GMC of seeps A and B reveals a large number of depressions and hummocky topographic features (Fig. 3b, c). While sites A and B are imaged with 3D seismics, only site B is imaged by both the 3D and 2D, HR seismic surveys (blue lines in Fig. 3d); we therefore focused this study on the better constrained southern site. An extensive fluid seepage system also develops along minibasins axis as demonstrated by the occurrence of conical and aligned seafloor pockmarks (Fig. 3).

The seepage zone located at the vertical projection of the GMC of seep B consists of a large (0.17 km^2) disturbed area (1200 m long and 300 m wide) forming a peapod-like feature on the seafloor. This zone defines an elongate cluster depressions (Fig. 4a) in trend with the eastern edge of the underlying salt diapir.

The entire depression complex is composed of 38 individual depressions, either isolated or merged, with diameters ranging from 25 to 100 m and depths ranging from one to 12 metres. Seafloor depressions correspond to high positive amplitudes extracted from the first arrivals of the 3D seismics (Fig. 4b).

Individual high-amplitude anomalies on the seafloor reflectivity have diameters ranging from 10 to 30 m and correspond to the bottom of individual depressions identified on the HR bathymetry (Fig. 4c). Seafloor reflectivity anomalies (10 – 15 m wide) located at the edge of the depression complex correspond to slight seafloor disturbances barely detectable on HR bathymetry. The high amplitude patches extracted from 3D seismics are coherent with high-density reflectivity anomalies visible on backscatter data

A large number of sub-circular mounds, up to 20m in diameter and less than 1 m high, occur outside the peapod-like depression complex (Fig. 4 d, g). Mounds are spread over a 900 m-wide area outside the depression complex. Seafloor mounds mostly gather into two main regions (Fig. 4 d, g) located in the internal zone inwards the diapir-affected area (see location in Fig. 3d). The northern and southern concentration areas are composed of 120 and 180 individual mounds covering seafloor areas of approximately 0.2 and 0.5 km², respectively. Mound density significantly decreases away outside these two areas. In the northern area, mounds form a cluster (Fig. 4d) that is associated with a slight increase of the seafloor amplitude (Fig. 4e). In the southern area, the seafloor is characterised by a low-amplitude area (Fig. 4h) and seafloor mounds are distributed along NE-SW seafloor escarpments.

The top of seafloor mounds show high amplitude anomalies, whose morphology matches that of the mound, sub-rounded or elongated (Fig. 4f, i). On 3D seismics, the depression areas are well discernible from the strong positive amplitude anomalies while the mounded area is only detectable on the backscatter data (Fig. 4e, h).

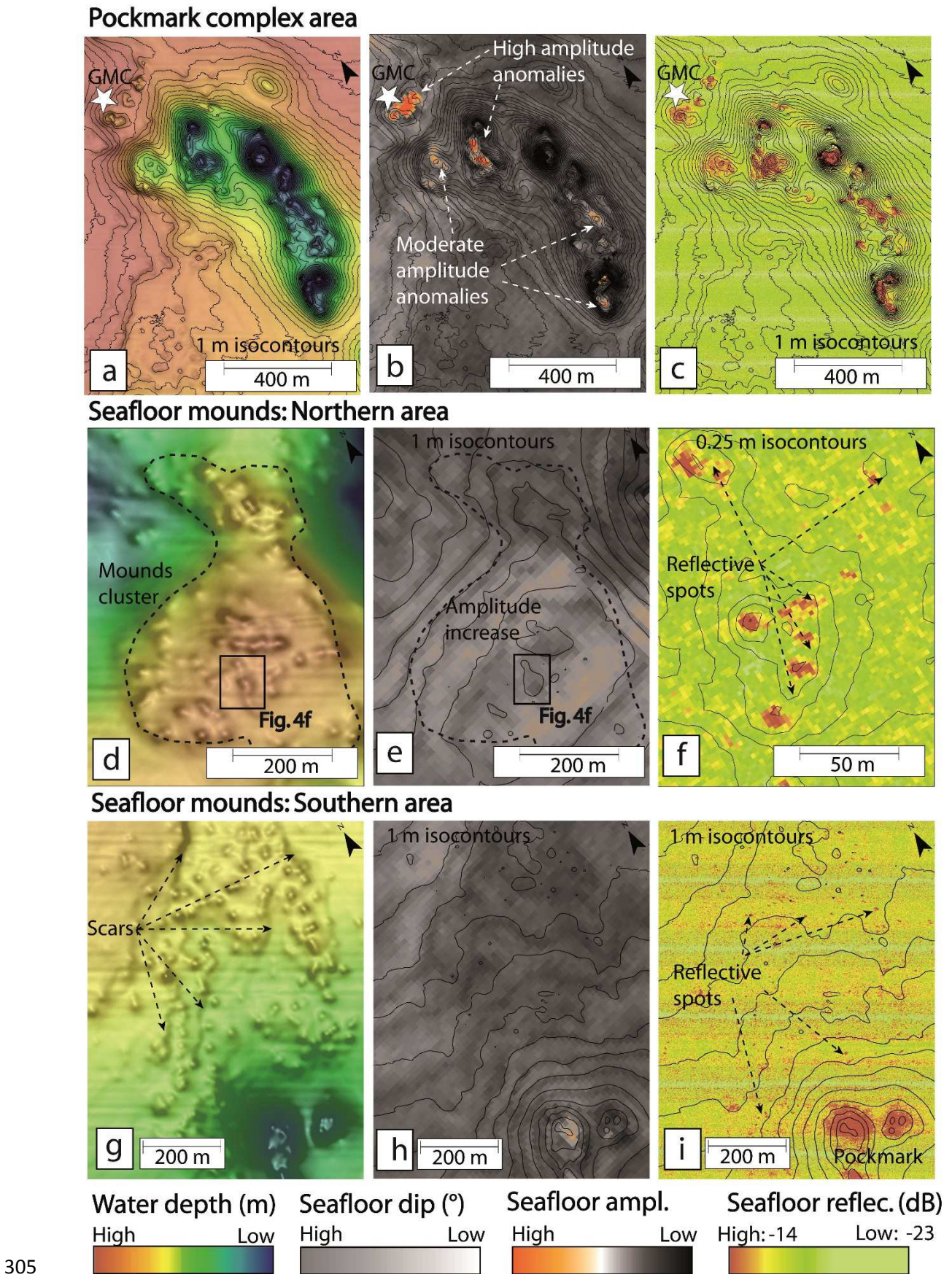
Pockmark complex area
GMC
1 m isocontours
400 m
a
GMC
High amplitude anomalies
Moderate amplitude anomalies
400 m
b
GMC
1 m isocontours
400 m
c
Seafloor mounds: Northern area
Mounds cluster
Fig. 4f
200 m
d
1 m isocontours
Amplitude increase
Fig. 4f
200 m
e
0.25 m isocontours
Reflective spots
50 m
f
Seafloor mounds: Southern area
Scars
200 m
g
1 m isocontours
200 m
h
1 m isocontours
Reflective spots
200 m
Pockmark
i
Water depth (m)
High
Low
Seafloor dip (°)
High
Low
Seafloor ampl.
High
Low
Seafloor reflec. (dB)
High: -14
Low: -23

305

Fig. 4: a. High-resolution seafloor bathymetry of the depression complex with gradient and 1-m isobaths contours overlain.. b. Amplitude map of the seafloor reflection from the 3D seismic block. c. Seafloor reflectivity map. d. Zoom on the bathymetry of the northern area of rough seafloor (see location in Fig. 3d). e. Amplitude map of the seafloor reflection from the 3D seismics superimposed with 1 m isobaths. f. Detail of (e) showing the increased seafloor reflectivity at the mound location. The map is overlain with 0.25 m isobaths. g. Seafloor map of the southern area of rough seafloor with 1 m-spacing isobaths contours overlain. h. Amplitudes of the first arrival at the seafloor extracted from the 3D seismics. i. Seafloor reflectivity map. Between high and low values, the bathymetry range is 20 m for (a) and (d) and 60 m for (g). See locations of the three boxes in Fig. 3d.

4.3. Sub-surface high amplitude reflection in the sub-bottom profiler data

In the SBP sections, high amplitude reflections are visible in the Quaternary series a few tens of ms below the seafloor (Fig. 5a) and are associated with acoustic attenuation below. The geophysical signature is similar to the High Impedance Layer (HIL) described and interpreted by ***Hill et al. (2010)*** as related to authigenic carbonate concretions. The lateral extension of the HIL reaches 2200 m across the SBP section over a 5.5 km² area (Fig. 5a, d) with a burial that varies from 0 to 100 ms TWT bsf. We differentiated three domains according to their position with respect to the underlying diapir: the central area that embraces the rugged seafloor depressions, the internal area covers the mounds-affected area and the external area outside the limits of the diapir. The geophysical signature of the HIL is the same throughout the affected area, but the relationship to stratigraphic boundaries differs between the three domains.

In the internal area, the top of the HIL corresponds to a sharp horizon. The TWT difference with the seafloor steeply decreases inwards (above the green dashed line in Fig. 5a, c) and remains buried 20 to 40 ms TWT below seafloor mounds (Fig. 5c, d and e). The HIL shows in many instances a layered character in trend with the stratigraphy around (Fig. 5a, b). Shallow faults, induced by the salt

tectonics deformation, disrupt the internal structure of HIL and connect the HIL slabs with seafloor mounds.

In the central area, the HIL burial substantially decreases along a 500 m wide stripe that follows the edge of the salt diapir (Fig. 5e). Local seafloor depressions are associated with high seafloor reflectivity values (Fig. 4b, c) and coincide with areas where the HIL reaches the seafloor (Fig. 5e) and columns of high amplitudes visible on the 3D seismics (Fig. 5b). The section displayed in Fig. 5a is in close proximity to seafloor depressions No. 1 and crosses depressions Nos. 2 and 3 (Fig. 5d). There, seafloor depressions are associated with an internal disorganisation of the HIL (see for instance Nos. 1 and 2 in Fig. 5a) and were coupled with a rapid acoustic wave attenuation.

In the external area, the HIL burial progressively increases outwards (Fig. 5e). A dominant crosscutting reflection marks the upper HIL boundary. The internal structure organises as thinned reflections aligned with the stratigraphy and pinched at the sideward HIL termination.

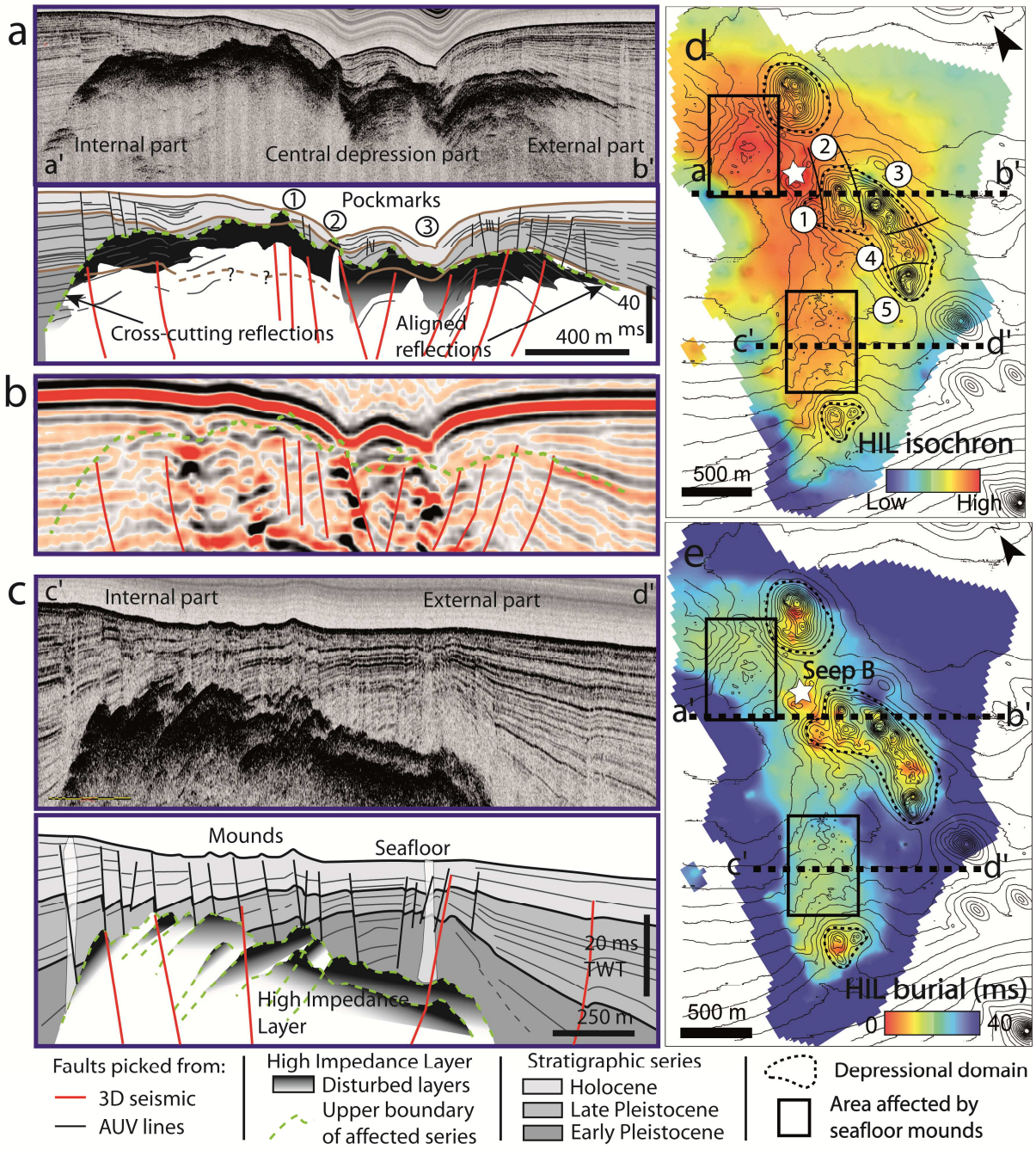

Fig. 5: a. SBP section (2D lines) displayed in envelope attribute through the High Impedance Layer (HIL) and interpretative line drawing. b. Seismic section of the shallow subsurface extracted from the 3D seismics, the layout was adjusted to fit with the SBP section in Fig.8a. The top of the HIL is shown with a dashed green line. c. SBP section displayed in envelope attribute and interpretative line drawing through the area affected by seafloor mounds. The interpretation section shows the association between sub-bottom HIL, seafloor mounds and shallow/deep faults. d. Map of the top

of the HIL picked from the 175 m separated SBP tracklines, the map is complemented with interpretative 3D picking between 2D sections considering seafloor reflective patches, fault trends or structural elements; 1m isocontours from multibeam bathymetry are overlain. e. Burial map of the HIL computed as the difference between the seabed reflection from 3D interpretation and the gridded top of the HIL.

4.4. Echo-characterisation of the seeping zone on the exploration seismic

On 3D exploration seismics, the TWT difference between the top of the diapir and the seafloor varies between 230 and 550 ms TWT (~195 to 465 metres below seafloor for an estimated propagation velocity of 1700 $m.s^{-1}$). Oil seeps from the shallowest part of the diapir area, i.e. where the sedimentary overburden is the thinnest (Fig. 6). Two specific seismic anomalies affect the Pliocene/Quaternary overburden at the crest of the salt diapir: (i) Positive high amplitude reflections and (ii) a double reflection with a polarity opposite to that of the seafloor (Fig. 6). Except in the internal part where seismic horizons continuity is disturbed, the 3D seismics is almost insensitive to the presence of the HIL depicted from the SBP dataset (see green dashed lines in Fig. 5b).

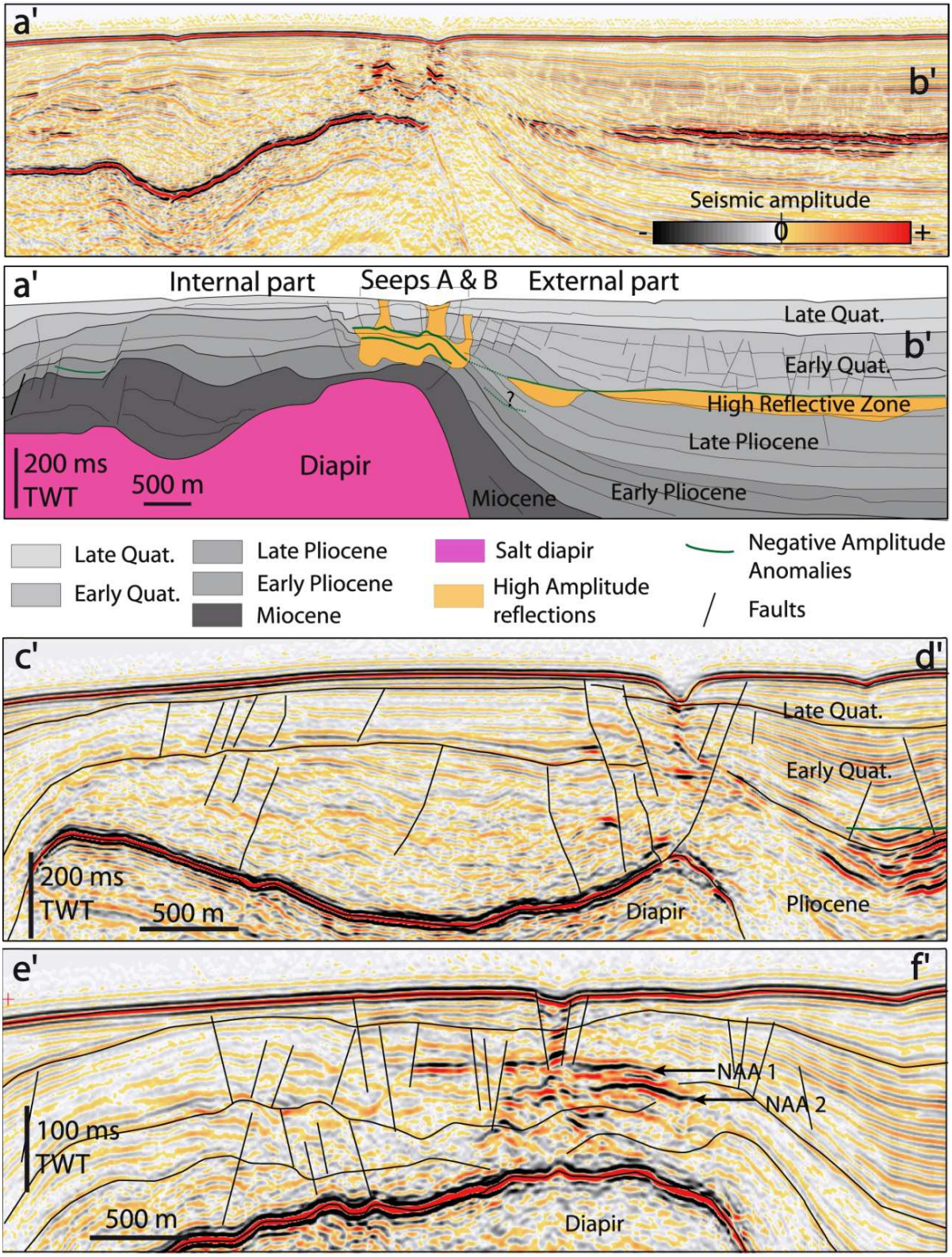
a'
b'
Seismic amplitude
-
0
+
a'
Internal part
Seeps A & B
External part
Late Quat.
Early Quat.
b'
High Reflective Zone
Late Pliocene
Early Pliocene
Miocene
Diapir
200 ms
TWT
500 m
Late Quat.
Early Quat.
Late Pliocene
Early Pliocene
Miocene
Salt diapir
High Amplitude reflections
Negative Amplitude Anomalies
Faults
c'
d'
Late Quat.
Early Quat.
200 ms
TWT
500 m
Diapir
Pliocene
e'
f'
NAA 1
NAA 2
100 ms
TWT
500 m
Diapir

364

Fig. 6: Seismic reflection sections and line drawing extracted from the 3D seismics (data courtesy of Total) showing a seabed and sub-seabed feature that SAR images indicate as currently leaking oil (see location of seismic sections in Fig. 3).

4.4.1. Negative Amplitude Anomalies

A strong Negative Amplitude Anomaly (NAA) characterised by a negative trace polarity compared to the seafloor reflection affects the seeping zone (Fig. 7a, b). The NAA1 (12.5 km²; Fig. 7c) mimics the shape of the diapir under the seeping zone and extends eastwards in relation to a deeper salt ridge that forms an anticline of the Neogene to Mid-Pliocene series in the minibasin. The horizon surface gently crosscuts stratigraphic boundaries, except below the depression complex, where NAA1 presents multiple local-scale upward deflections. The vertical position of NAA1 from the seafloor is roughly 200 m (~295 ms TWT) shallower above the diapir compared to the minibasin over a distance of 6000 m apart. The area is also characterised by a deeper, moderate but consistent NAA2, with an extent of roughly 1.1 km² over two separate areas at the location of seafloor local depressions (Fig. 7d). NAA2 is almost parallel to NAA1 from a distance of about 20 ms TWT and is also deflected upward below the locations of local depressions (Fig. 7e).

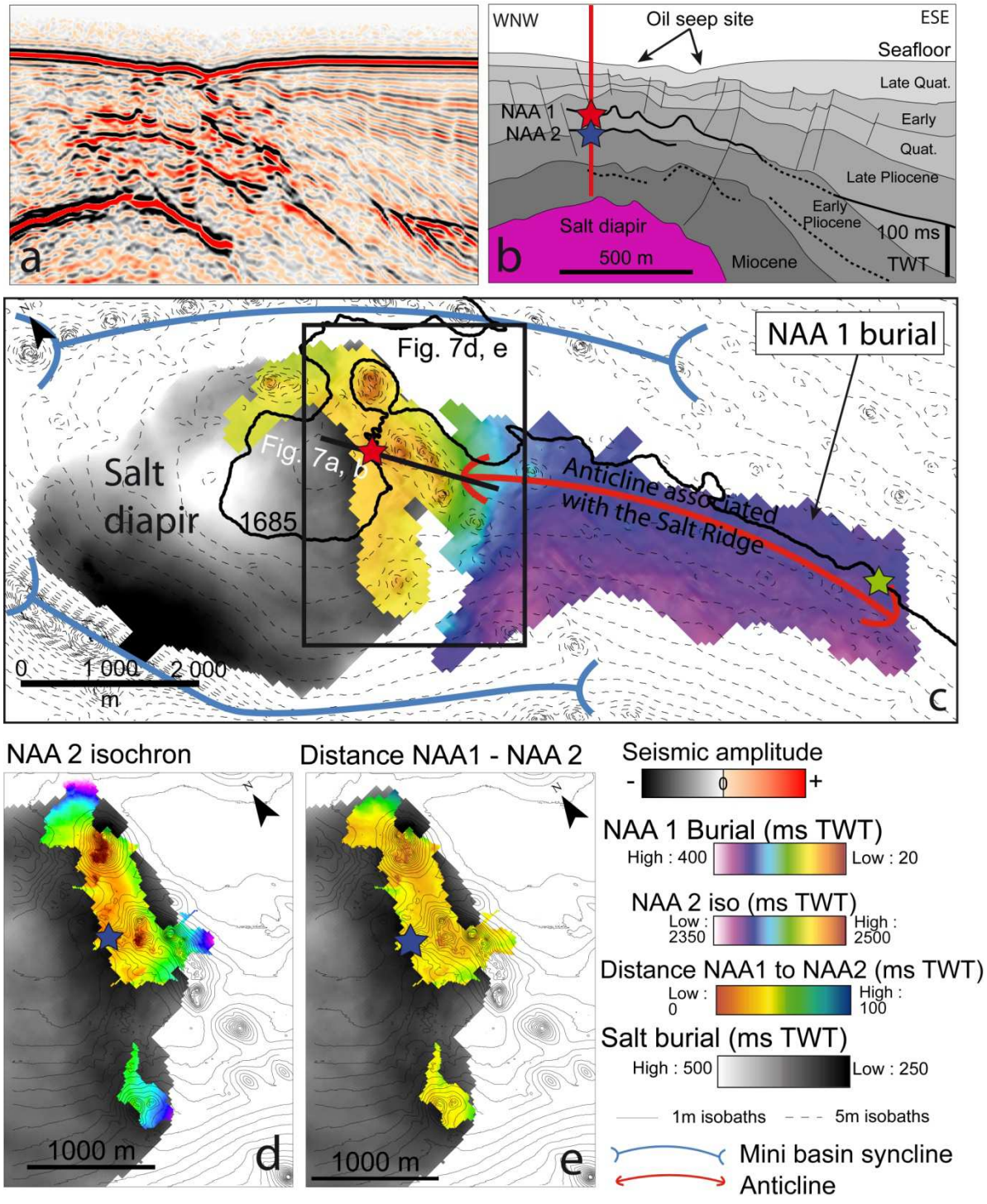

380

381 **Fig. 7: a. Exploration seismic section of the subsurface bypass system above the salt diapir showing**
382 **the seafloor depression complex and the two negative amplitude reflections NAA1 and NAA2 (see**
383 **location in Fig 9c). b. Interpretative line drawing. c. Map of the extent of NAA1. Salt burial is**
384 **displayed in greyscale. Black dashed lines are 5 m isobaths. d. Picking of the extent of NAA2 (see**

location in Fig. 7c). The colour scale refers to the burial between the seafloor and the negative polarity reflection. e. Map of NAA1 to NAA2 isochron.

4.4.2 Three dimensional distribution of high amplitudes

The interval from the HIL to the salt diapir is affected by High Amplitude Bodies (HAB) below the seeping zone (Fig. 8a). The high amplitudes occur as two distinctive features vertically delimited by NAA1 (Fig. 8a). The first is expressed by consistent and massive HAB in close proximity to the salt diapir (Fig. 8b), covering an area of 2.8 km². The second one consists of a vertical succession of local and focused amplitude anomalies corresponding to pipe-like features rooted on the massive HAB (Fig. 8c). NAA1 delimits the massive HAB at the top and acts as a transition horizon to the pipe-like features layer (Fig. 8a). The seismic pipes consist of a vertical succession of high amplitude anomalies stacked through roughly 50 to 100 ms (maximum of 85 m of sediments) with diameters ranging from 65 to 220 m. We identified 16 individual pipes near the oil seep site (Fig. 8c).

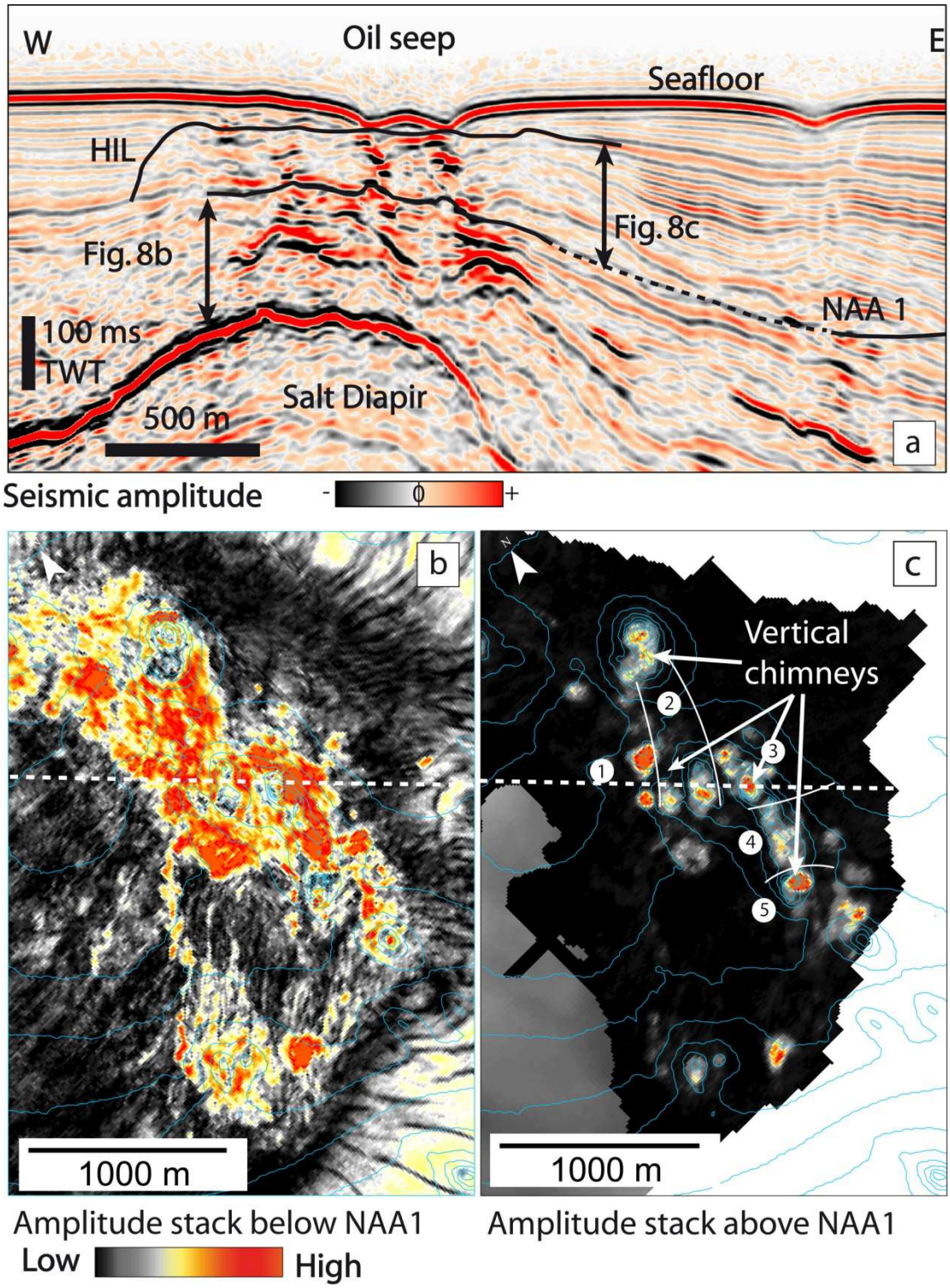

Fig. 8: a. Seismic section below the depression complex (see location in white dashed line in Fig. 10b, c). The map is superimposed with NAA1 and HIL horizons in black lines. b. Map of the RMS amplitude stack on the interval between seafloor + 100 ms and 200 ms TWT corresponding to the

layers below NAA1. c. Map of the RMS amplitude stack between the HIL and NAA1. The RMS amplitudes are superimposed with seafloor 5 m interval contour lines.

4.4.3. Fault network below the seeping zone

Deformation related to salt tectonics results in the development of a fault network at the crest of the diapir that is exclusively produced by normal faults. With respect to the diapir, one family is clearly radial (green in Fig. 9) while the others are concentric (blue, orange and red). The seeping zone is located at the junction of concentric and radial fault networks. The concentric fault families, composed of conjugate and converging faults (in red and blue), are mostly rooted on the diapir, triggering the development of a local mini-graben along the salt rim.

We carried out a multi-scale recognition of the fault network using a combination of 2D and 3D seismics (Fig. 9b). In some cases, faults identified on the SBP sections propagate deeper on the 3D exploration seismics (Fig. 5a, b, c). The seafloor scars show that most of the concentric faults are still active (Fig. 4 and Fig. 5).

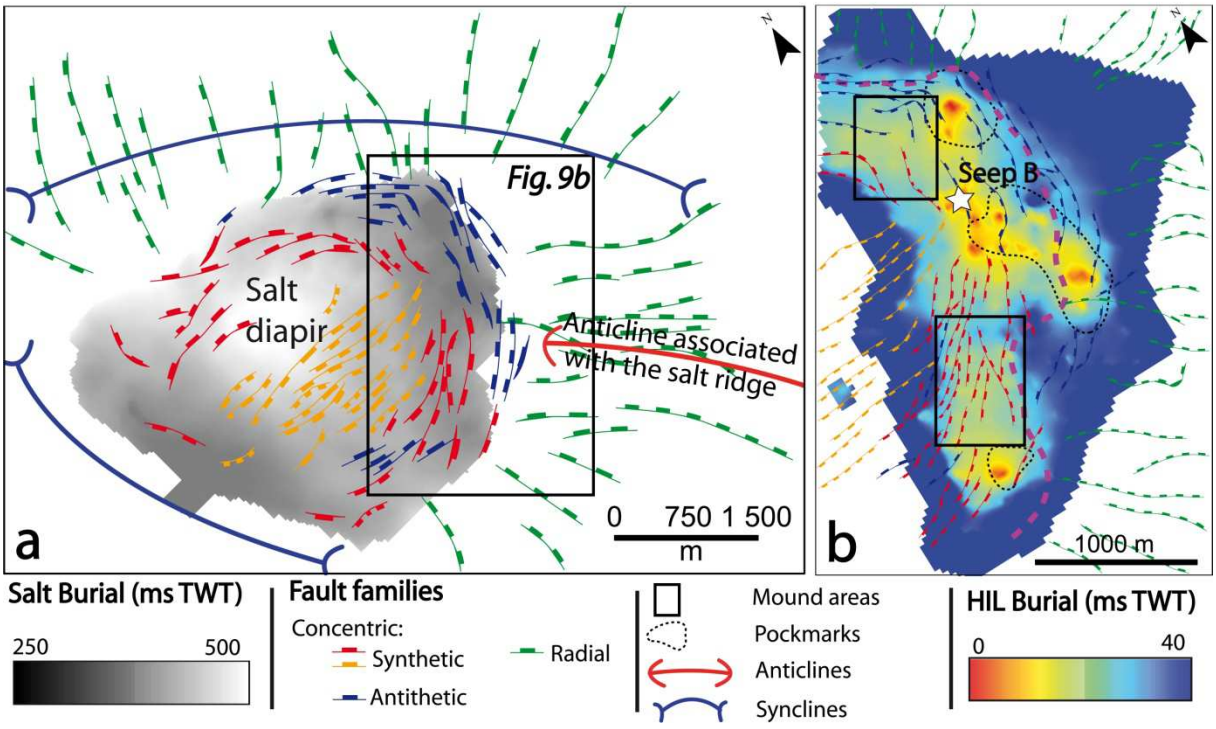

414

415 **Fig. 9: a. Inventory of shallow faults picked from 3D seismics. The faults are sorted between four**
416 **main families of normal faults composed of gravity collapse (orange), synthetic concentric faults**
417 **(red), antithetic concentric (blue) and radial (green). b. Seafloor faults picked from the combined**
418 **analysis of seafloor imagery, SBP sections and 3D seismics. The map is superimposed with HIL**
419 **burial, location of the seafloor depression complex and asphalt mound areas.**

420 # 5. Interpretation, discussion and implications

421 ## 5.1. Linking sea surface and seafloor observations

422 Miscellaneous hydrographical components affect the hydrodynamic conditions of the LCB, which
423 potentially induce opposite deflections across the water column (***Peterson and Stramma, 1991;***
424 ***Schneider et al., 1996; Holmes et al., 1997; Stramma and England, 1999; Shannon, 2001; Hardman-***
425 ***Mountford et al., 2003; Hopkins et al., 2013; Jatiault et al., 2018***). The OSO dispersion remains low
426 (<1500 m around the emission point; Fig. 3a) suggesting that the deflection of OSO is restricted to
427 low horizontal distances, even if the direction is highly variable. Low deflections are presumably due

428 to the effect of opposite current components at different water depths. Modelled deflection
429 distribution shows that the average surfacing area roughly corresponds to the vertical projection of
430 seafloor source as suggested by the literature near this study area (***Jatiault et al., 2018***). The
431 computation of the average location of the OSO is relevant under the conditions of abundant of slicks
432 emissions and the uncertainty associated with the location of the origin of the oil on the seafloor is
433 significantly reduced when the slicks collection is important. For a large number of the 28 slicks for
434 seep B, we consider that the sub-vertical projection of the GMC provides a satisfactory
435 approximation of the origin of the oil on the seafloor (Fig. 3) with a degree of uncertainty between
436 100 and 200 m. The vertical projection of the GMC to the seafloor of seep site A corresponds to the
437 lateral extension of the seeping zone and presents similar characteristics on the 3D seismics (HAB
438 below the NAA1 linked to vertical pipes and seafloor irregular depression).

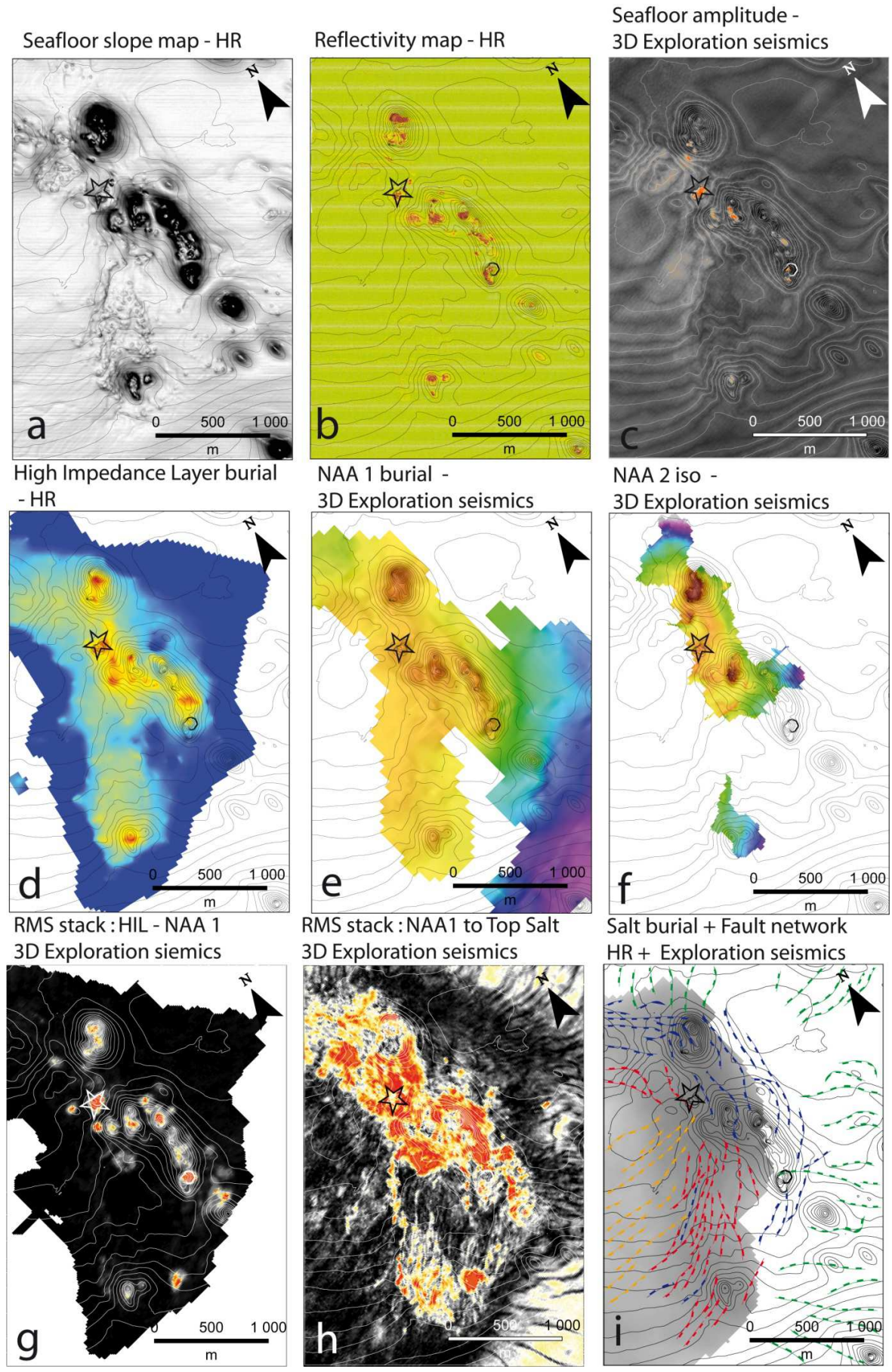
Seafloor slope map - HR
Reflectivity map - HR
Seafloor amplitude -
3D Exploration seismics
a
b
c
0 500 1 000
m
High Impedance Layer burial
- HR
NAA 1 burial -
3D Exploration seismics
NAA 2 iso -
3D Exploration seismics
d
e
f
RMS stack : HIL - NAA 1
3D Exploration siemics
RMS stack : NAA1 to Top Salt
3D Exploration seismics
Salt burial + Fault network
HR + Exploration seismics
g
h
i

439

Fig. 10: Overview of key horizons picked from the combination of the HR survey and 3D seismics. The maps are superimposed with 1 m isocontour a. Seafloor slope map. b. Reflectivity map. c. Seafloor amplitude map. d. Map of the HIL burial. e. Isochron map of NAA1. f. Isochron map of NAA2. g. Stack of the RMS amplitude from the HIL to NAA1. h. Stack of the RMS amplitude from NAA2 to the top salt. i. Salt burial superimposed with fault network picking.

5.2. Lateral evolution of seepage intensity: Focused vs distributed

5.2.1. Geophysical evidence for focused fluid flow

The combination of the 3D seismics and the high-resolution survey data is meaningful to correlate seafloor characteristics (Fig. 10 a, b and c), key horizons depths in the subsurface (HIL; Fig. 10 d) and at deeper series (NAA1, NAA2, HAB; Fig. 10 e, f, g, h).

The recognition of negative polarity reflections crosscutting stratigraphic series under the condition of abundant hydrocarbon migration is largely recognised as being associated with the Base of the Gas Hydrates Stability Zone (BGHSZ) but can also be considered as the opal A/CT transition (***Berndt et al., 2005)***. Different studies already reported a hydrate-related BSR (Bottom Simulating Reflection) in the LCB (***Lucazeau et al., 2004; Gay et al., 2006b; Andresen et al., 2011; Andresen, 2012; Nyamapfumba and McMechan, 2012; Wenau et al., 2014a, b***) where leakages form gas accumulations that feeds the BSR above. The presence of a high-reflectivity zone (HRZ - ***Andresen et al., 2011***) below NAA1 in minibasins suggests that the gas is trapped beneath the impermeable BSR (Fig. 6). We converted the time recorded between the seafloor and NAA1 to estimate the geothermal gradient above the diapir using a speculative linear propagation velocity. The distance between the seafloor and the BSR provides a means to estimate the geothermal gradient assuming that the temperature is constant at the seafloor (4 °C) and as a function of the depth (P-T) at the BSR level. In order to compute a straight comparison of the geothermal gradient in sediments, we selected areas where the water depth is equal between the diapir and the minibasin areas (1685 m; Fig. 7c).

464 Considering a propagation velocity of 1500 to 1700 $m.s^{-1}$ in the shallow sediments, we estimate that
465 the BSR depth is comprised between 1915 to 1945 m in the minibasin (green star in Fig. 7b, c) and
466 between 1760 to 1770 m above the diapir (red star in Fig. 7b, c), which corresponds respectively to
467 geothermal gradients between 143 and 162 $°C.km^{-1}$ above the salt diapir and between 50 and 57
468 $°C.km^{-1}$ in the minibasin (green star in Fig. 7c). This estimation is 100m shallower than the theoretical
469 depth of the opal A/CT transition and rather corresponds to the reported range of a hydrate-related
470 BSR in the area (***Serié et al., 2016***) and therefore confirms that the actual BGHSZ is a good candidate
471 to explain NAA1. The BGHSZ depth primarily depends on Pressure-Temperature conditions, the gas
472 type (***Sloan, 1990; Sloan, 2003***), the gas flow and to a lesser extent on water salinity. The thermal
473 conductivity of evaporites (~6.5 W/m.K) is greater than the surrounding siltstones and shales (1.5 -
474 2.5 W/m.K - ***Serié et al., 2016***) and the heat is more efficiently conducted from deeper series across
475 evaporites series, which result in a thermal anomaly below the seafloor. The proximity of the
476 underlying evaporites decreases the hydrate stability interval by (1) increasing of the NaCl
477 concentration (***Sloan 2003; Qi et al., 2012; Chong et al., 2015***) and (2) creating a positive thermal
478 anomaly (***Lucazeau et al., 2004***). The extension of NAA1 towards the minibasin suggests that a
479 considerable amount of gas migrates laterally along the BGHSZ from the minibasin towards the peri-
480 diapiric areas (Fig. 6). The sub-circular local-scale upward deflections of the BGHSZ evidences local
481 thermal anomalies associated with an active flow of warmer fluids along focused migration paths
482 (***Gay et al., 2006 b***), which also corresponds to the upward deflections area of the NAA2 (Fig. 10 f).

483 The vertical high amplitude pipes connects the BSR with seafloor depression areas on the 3D seismics
484 and are therefore interpreted as deep feeder conduits for fluids throughout the sedimentary pile.
485 This suggests that the hydrocarbon flow is focused and consistent above the BGHSZ (Fig. 10 g).
486 Massive HAB induces an acoustic mask, which prevent the recognition of potential vertical conduits
487 below (Fig. 10 h). The acoustic response of vertical pipes visible on exploration seismics corresponds
488 to the disorganised, seafloor-reaching HIL on the SBP sections (Fig. 10 d) and coincides with the

489 locations of seafloor high amplitude anomalies, the high amplitude pipes on 3D seismics (Fig. 10g)
490 and the depression complex location (Fig. 10a, b, c).

491 The location of the depression complex is fairly well oriented along the salt diapir and at the
492 intersection area of most of faults families (conjugate concentric and radial faults; Fig. 9a), suggesting
493 a sub-vertical migration of fluids along peri-diapiric conjugate faults (Fig. 10 i). The connection with
494 deeper faults suggests that fluids may migrate along structural trends from deeper series (Fig. 5).

495 Seafloor depressions are typical features of focused fluid flow (***Hovland and Judd, 1988, Paul and***
496 ***Ussler, 2006, Roberts et al., 2006; Ho et al., 2012***) usually entitled as pockmarks (***King and McLean,***
497 ***1970***). In the case of seepage disruption, the depressions progressively get in-filled with sediment
498 (***Cifci et al., 2003; Hovland et al., 2010; Ho et al., 2012***). Their persistence therefore suggests an
499 active flow. The spatial correspondence of seafloor pockmarks (Fig. 10a) within the depression area,
500 seafloor backscatter anomalies (Fig. 10b), seafloor amplitude anomalies (Fig. 10c), vertical pipes and
501 upward deflection of the BSR, provides strong evidence of active or recent important and focused
502 fluid flows through multiple conduit outlets. The seepage activity is therefore evidenced for the 38
503 individual depressions. The present-day activity throughout multiple fluids outlets therefore creates
504 a cluster of heterometric pockmark (Fig. 4c). Oil bubbles, are commonly expelled as oily-coated
505 bubbles with an important volume of lighter gas to rise towards the sea surface (***Körber et al., 2014***).
506 The fluid migration mechanism seems to be erosive in the depression complex, probably due to
507 sediment liquefaction associated with considerable oil and gas flows at focused seep sites, which
508 therefore constitute the main seafloor source of oil slicks visible at the sea surface. Accordingly, the
509 locations of the GMC for seep A and B correspond to the focused seep sites in the paper (seafloor
510 depressions).

5.2.2. Geophysical evidence of peripheral dispersed fluid flow

Several geophysical observations suggest that the fluid flow strongly decreases away from the main conduits described before. The presence of fluid-related geophysical anomalies such as NAA1 or HIL suggests that fluids migrate outwards the main fluid conduit at the depression areas (Fig. 10 d, e and i). In the internal area, the mound formation mechanism is a constructive/non-erosive mechanism (Fig. 4). The absence of erosive seafloor features (i.e. pockmarks) associated with gas erosion/ fluidization, coupled with buried HIL (Fig. 10 d) suggest that the portion of gas is sufficiently low to be entirely consumed with the anaerobic oxidation of methane reaction (**AOM :** $\boldsymbol{CH_4 + SO_4^{2-} => HCO_3^- + HS^- + H_2O}$; e.g. ***Hovland et al., 1987; Hovland and Irwin, 1992***) or by hydrate nodule formation (***Hovland and Svenssen, 2006***). Constituent materials of meter-scale seafloor mounds (Fig. 10a) differ from the surrounding siltstones based on the seafloor reflectivity anomalies. Recent studies that investigated similar restricted-size mounds with ROV dives in the same area (***Unterseh, 2013; Jones et al., 2014***) showed hardened extruded asphalts resulting from the severe biodegradation of hydrocarbons compounds under the action of bacteria in the shallow subsurface (***Head et al., 2003; Larter et al., 2003; Larter et al., 2006; Peters et al., 2007***). Two hypotheses could explain the seafloor scattering of mounds distribution. The first proposes a density-driven storage of hydrocarbon at the sediment/water interface due to a biodegradation-induced density increase, following a migration stage across sediments. The second involves a vigorous expulsion stage of the asphalt material in the water column and a lateral transportation by bottom currents later followed by a distant deposition on the seafloor. The latter is possible but restricted to a few tens of metres from the outbreaking area (***Jones et al., 2014***) while closest pockmarks are separated by at least 500 m from the asphalt mound fields (Fig. 10 a). In addition, the distribution of asphalt mounds compared to pockmark locations are opposite to the main bottom current (***Geldof et al., 2014***). In the southern area the spatial concurrence of asphalt mounds and salt-related seafloor scarps (Fig. 10 a, i), together with vertical offsets of stratigraphic series on top of the HIL suggests that asphalt

mounds are directly emplaced above migration pathways and that faults guide oil from the HIL to the seafloor (Fig. 5c).

The presence of heavy oils on the seafloor, such as tar or asphalt mounds (***Keller et al., 2007; Valentine et al., 2010***), indicate that biodegradation is severe and that the oil dysmigration process is a relatively slow process. The combination of buried HIL, NAA1 and asphalt mounds in the internal area suggests that the hydrocarbon migrates towards the sea surface but that the migration process is slower compared to the main conduits, evidencing a low-flow/dispersed migration area. The development of a main fluid conduit together with peripheral and auxiliary pipes was already reported at the sample scale for gas migration through a water-saturated sediment pile (***Cuss et al., 2014)***. Multiple conduit outlets were also observed in this study from a large number of pockmarks and asphalt mounds (Fig. 4) that developed in relation to the fault network (Fig. 9).

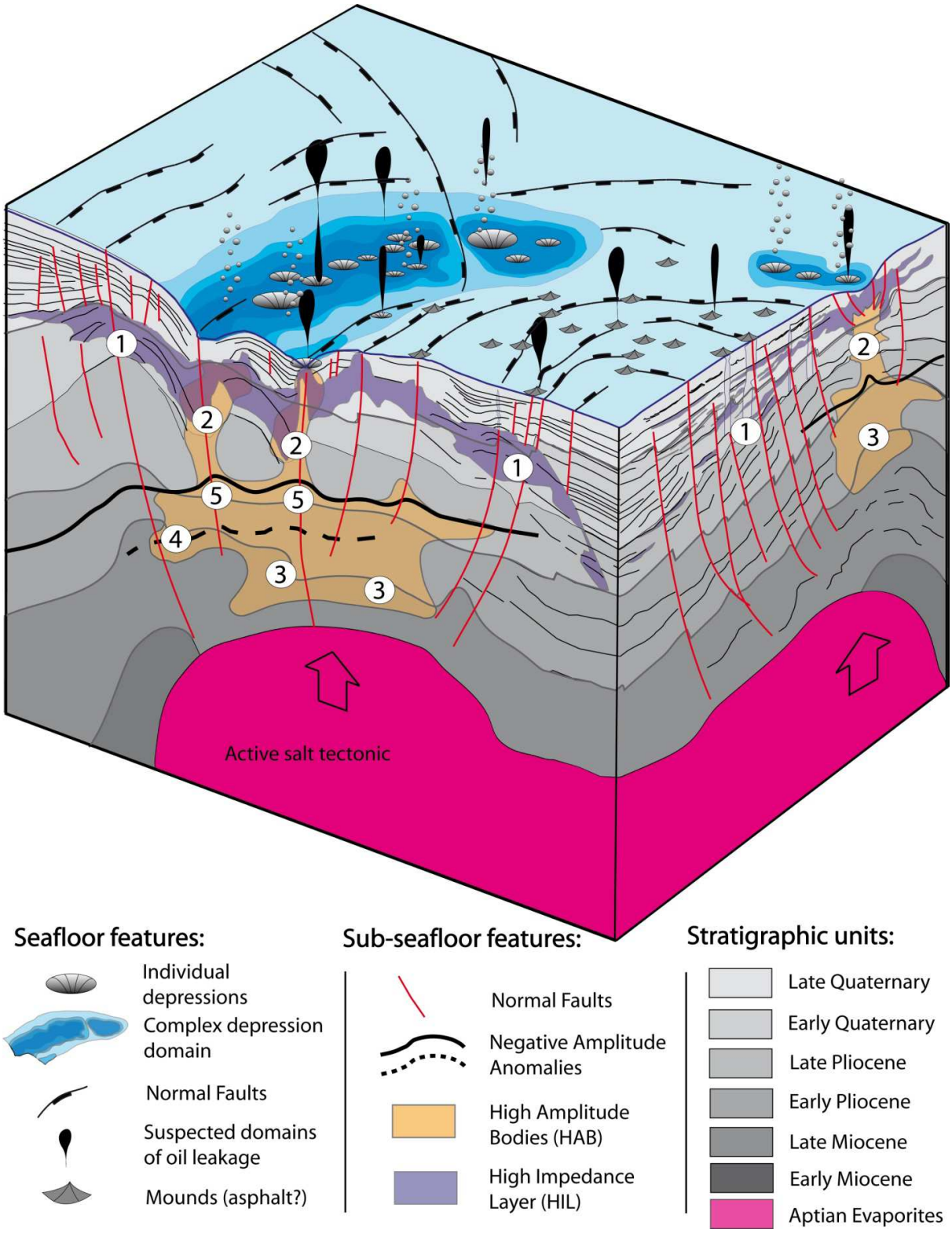

547

548 **Fig. 11: Diagram of the synthesis of the geophysical and geological attributes associated with the**

549 **studied thermogenic seep complex, based on the analysis of SBP sections and 3D seismics.**

5.3. Significance of positive geophysical anomalies

5.3.1. Significance of the conformable HIL

The AOM results in the development of methane derived authigenic carbonates (MDAC) known to generate strong seismic reflections (e.g. ***Heggland, 2002; Judd and Hovland, 2009; Petersen et al., 2010; Andresen et al., 2011; Ho et al., 2012***) due to the competence contrast with the surrounding fine-grained siltstones. Authigenic carbonates and can probably be interpreted as the main component of the conformable HIL (No. 1 in Fig. 11). The hydrocarbon flow controls both the proximity with the seafloor where carbonate precipitates (namely, the sulphate methane interface; SMI) and the size of carbonate concretions (***Paull and Ussler, 2008***). In the case of moderate flow, carbonates precipitate as restricted-size concretions with a substantial distance from the seafloor. The SMI typically varies in depth between less than a metre and a few tens of metres, although exceptional values of several hundred metres were reported (***Borowski et al., 1999; Ivanov et al., 1989; Dikens, 2001; Arning et al., 2015***). Carbonate concretions were reported in the LCB with sizes ranging from cm to dcm (***Pierre and Fouquet 2007; Feng et al., 2010; Hass et al., 2010; Thomas et al., 2011***). This may explain that HIL are not detected with the resolution of the 3D seismics but well imaged with the cm scale SBP resolution (Table. 1). The association of shallow faults, asphalt mounds and HIL suggests that the asphalt material transits through the HIL (***Hill et al., 2010***). Solidified crude oil might also generate a shallow acoustic reflection and conformable HIL are probably composed of a mix of asphalt material and restricted-size carbonate concretions, where carbonate slabs act as a temporary reservoir/cap rock system for asphalt materials (Fig. 5).

5.3.2. Vertical high amplitude pipes

High amplitudes anomalies below pockmarks (No. 2 in Fig. 11) are usually interpreted in the literature as authigenic carbonate concretions that form close to the seafloor (***Léon et al., 2006; Römer et al., 2014***). In this case, the observed high amplitude pipes may correspond to a vertical

succession of carbonate crusts formed at successive paleo seafloors. The diameter of seismic pipes (100 - 220 m) is widely above the maximum of reported decimetric-scale ground-truth carbonate chimneys (***De Boever et al., 2006; Nyman et al., 2006***) and likely corresponds to carbonate chimney clusters. The geophysical signature of near-seafloor hydrates remains under-documented but it appears as consistent and disorganised high amplitude anomalies in the Northern Congo Delta (***Zülhsdorff and Spiess, 2005***), which present similar geophysical signature to the disorganised/seafloor-reaching HIL. Vein-filling hydrate enrichment presumably enhances the impedance contrasts in the fine-grained shallow sediments and could be an alternative explanation for the observed high amplitude vertical pipe (***Riboulot et al., 2016***), both in the sediments and at the seafloor.

5.3.3. Massive high-amplitude bodies: A contribution of anhydrite dissolution?

The massive HAB below NAA1 (No. 3 in Fig. 11) can be explained as a temporary storage of hydrocarbon fluid below the impermeable BGHSZ (***Sloan, 2003***), while the structural trap is induced by the salt-related thermal anomaly (***Calvès et al., 2008; Serié et al., 2016***). However, the presence of gas is associated with negative polarity reflections while the amplitude anomalies reflections observed close to the diapir are positive (Fig. 8b). The Aptian evaporites were reported to be composed of halite and potash salt topped by anhydrite in the study area (***Teisserenc and Villemin, 1989; Brownfield and Charpentier 2006; Anka et al., 2009***). The sulphate reduction in association with the anhydrite dissolution ($CaSO_4 + CH_4 \rightarrow CaCO_3 + H_2S + H_2O$) is effective in the presence of hydrocarbons (***McKelvey, 1986; Fontboté 1994; Seawald, 2003***) and produces a cap rock partly composed of calcite and hydrogen sulphur (***MacKelvey, 1986***). This reaction takes place both at high temperature (100 to 180 °C) by the thermochemical sulphate reduction (***Warren, 2000; Machel 2001; Seewald, 2003; Cai et al., 2004; Fu et al., 2016***) and at lower temperature (0 to 80 °C) under bacterial sulphate reduction (***Machel, 2001; Stafford, 2008***). Anhydrite is known to be commonly present within the salt diapir cap rock together with calcite (***Posey et al., 1987; Sassen et al., 1994;***

Jackson and Lewis, 2012; Warren, 2016), as reported along Gabonese (***Teisserenc and Villemin, 1989***) and Angolan basins (***Brownfield and Charpentier, 2006; Gindre-Chanu et al., 2015***). We propose that anhydrite dissolution in the condition of abundant hydrocarbon migration could explain the high positive amplitudes anomalies observed close to the salt diapirs in offshore Angola. The storage of hydrocarbons below the BGHSZ probably helps to satisfy the necessary persistence of hydrocarbon presence required for carbonate precipitations.

5.4. Significance and implications of the double Negative Amplitude Anomaly

Multiple observations of stacked BSR were already reported in multiple continental margins and in varied context (***Posewang and Mienert, 1999; Andreassen et al., 2000; Foucher et al., 2002; Bangs et al., 2005; Popescu et al., 2007; Cullen et al., 2008; Gelleti and Busetti, 2011; Huuse et al., 2014).*** The observation of multiple BSR however remains occasional and still controversial. Three main hypotheses are considered to explain the second BSR. The first refers to the transition between opal A and opal C/T that creates a cross-stratal reflection with a positive amplitude contrast (***Davies and Cartwright, 2002; Lee et al., 2003; Cartwright et al., 2003; Berndt et al., 2004***). This hypothesis is unlikely assuming that (i) the amplitude contrast is supposed to be positive, conversely to our case study (Fig. 7a), (ii) the Quaternary series are only characterised by fine-grained/silica-poor siltstones and (iii) considering environmental conditions, the opal A/CT transition should be at least 100m below the actual BSR in the minibasin. Alternatively, a vertical displacement of the BGHSZ following environmental conditions modifications could generate a second BSR. Following a marine transgression, the enhancement of the hydrostatic pressure displace the BGHSZ location downward which enables the preservation of the previous BSR within a thicker stable hydrate interval (***Bangs et al., 2005***). However, sea level fluctuations would result in a regional modification of the stability conditions of gas hydrate and in a regional displacement of the vertical location of the BGHSZ. Local uplifts due to post-depositional deformations also potentially modify the depth of the BGHSZ where

624 the NAA2 could mark the former gas front below the BGHSZ (***Macmahon et al., 2014***). Ongoing salt
625 tectonics probably results in hydrate dissociation over time by progressively heating the overburden
626 (***Lucazeau et al., 2004; Serié et al., 2016***). Yet the paleo-location of the BSR is unlikely to produce a
627 seismic reflection below the actual BGHSZ under the condition of heating from the substratum. In
628 addition, the effect of salt tectonics deformation (comparable to the sedimentation rate; ~0.1 mm.yr^{-1}
629 ; ***Berger et al., 1998***) is insignificant compared to other external factors such as the potential
630 hydrostatic pressure variability (~ 7 mm.yr^{-1}; 120 m since the last glacial maximum 18 kyr ago; ***Lobo***
631 ***and Ridente, 2013***). Finally, the composition of expelled fluids modifies the thermodynamic
632 conditions of the gas hydrate stability. Compared to traditional hydrate structure I, structures II and
633 H are stable at greater depth and potentially host heavier hydrocarbons (***Sloan, 1990; Sloan, 2003***).
634 In the case of thermogenic seeps, multi-phased fluid composition could therefore result in multiple
635 BGHSZ, as suggested by several studies (***Andreassen et al., 2000; Macmahon et al., 2014; Pecher et***
636 ***al., 2014; Pecher et al., 2014; Li et al., 2015***).

637 This case study refers to two-stacked NAA, where the extent of the deeper NAA is restricted to the
638 active seeping area (No. 4 in Fig. 11). The identification of recurrent oil slicks at the sea surface
639 testifies thermogenic hydrocarbon migration and the location of NAA2 corresponds to the
640 thermogenic seeping zone (Fig. 7 c, d). In addition, the upward deflection testifies an active fluid flow
641 (***Gay et al., 2007***) is observed at both NAA (No. 5 in Fig. 11). The curves of the BGHSZ can be assessed
642 depending on the gas composition and P-T conditions (***Sloan, 1990)***.

643 We considered three different propagation velocities to estimate the geothermal gradient above the
644 diapir (Table 3):

645 1. A minimalistic velocity model using 1500 m.s^{-1} in the shallow subsurface;
646 2. A probable velocity model of 1700 m.s^{-1} assuming that the propagation velocity of acoustic
647 waves is enhanced at the crest of the diapir due to an outcrop of slightly older and compacted

sediments together with the presence of hydrate/carbonate related high amplitudes (HIL and HAB) and;

3. An upper threshold fixed at 2000 $m.s^{-1}$.

In the Kwanza basin, the geothermal gradient associated with salt diapir burial similar to this case study (~250 ms TWT bsf) was reported from 140 to 200 $°C.km^{-1}$ (***Serié et al., 2016***). The range is likely in agreement with the probable and minimalistic propagation velocity (Vp_1 and Vp_2 in Table 3). The gas composition of the depth of NAA2 (blue stars in Fig. 7b) is estimated from the projection on the P-T diagram of the geothermal gradient assessed from NAA1 inferred to be composed of 100% methane hydrates (red star in Fig. 7b).

Table 3: Estimation of the geothermal gradient computed using the time recorded between the seafloor and the BSR using 3 different propagation velocities.

	Minibasin		Above diapir		
	NAA1		NAA1		NAA2
Propagation velocity ($m.s^{-1}$)	305 ms TWT bsf		100 ms TWT bsf		133 ms TWT bsf
	Geothermal gradient ($°C.km^{-1}$)	Estimated Depth (m)	Estimated Depth (m)	Geothermal Gradient ($°C.km^{-1}$)	Estimated Depth (m)
Vp_1= 1500	56.9	1915	1760	162	1785
Vp_2= 1700	50.5	1945	1770	143.5	1798
Vp_3= 2000	-	-	1785	124	1813

For the three propagation velocities, the projection of the geothermal gradient for NAA2 (blue stars in Fig. 12) ranges in the stability conditions of thermogenic gas melt reported by ***Sloan (1990)*** and later used by ***Gelleti and Busetti (2011)*** and ***Li et al. (2015)***. The estimation of the gas composition using the "probable" velocity model and the upper threshold provides comparable results. The relative portion of heavier gas would range between 3 and 7% for ethane and between 1 and 3% for propane (Fig. 12).

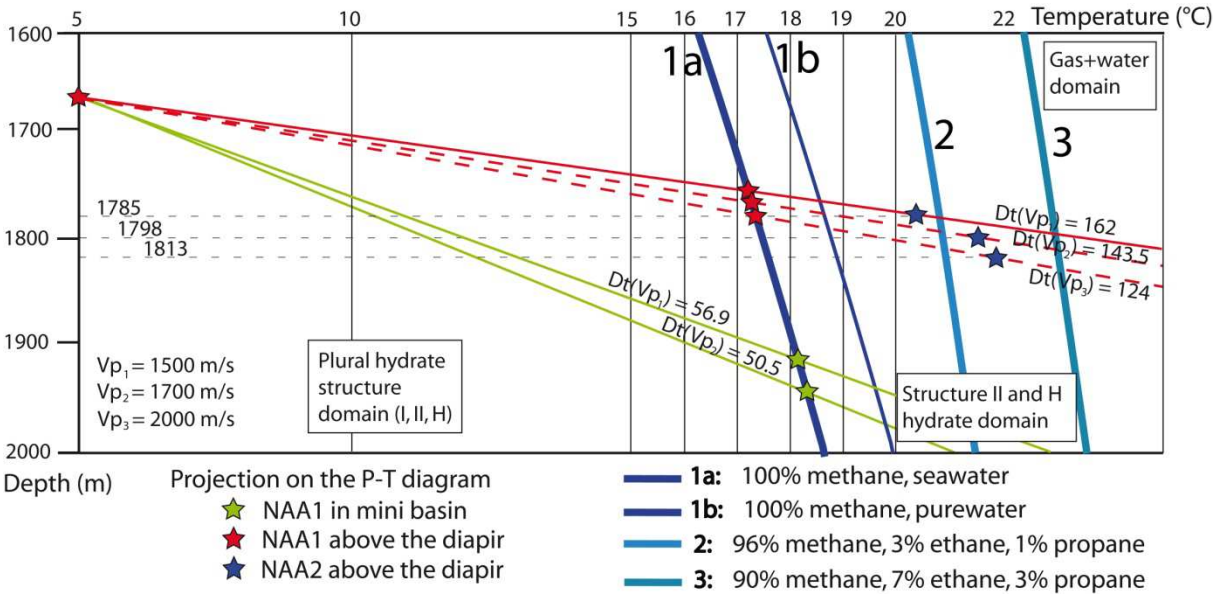

Fig. 12: Phase diagram and hydrate stability domains (Sloan, 1990). Green and red stars correspond to the projection in the P-T diagram of the estimated depth NAA1 for different propagation velocities in the minibasin and above the diapir, respectively. The slope of the line corresponds to the geothermal gradient, considering a seafloor depth of 1685 metres and 100% methane hydrate in seawater (see location of selected areas in Fig. 7). Blue stars correspond to the projections of NAA2 using the three geothermal gradients computed from the estimated depths of the NAA1 above the salt diapir.

5.5. Recognition criteria of an active thermogenic oil seeping area

The combination of different resolution scale geophysical datasets highlighted specific thermogenic seep features. High amplitudes in both the SBP and 3D exploration seismics appear as a relevant feature to identify hydrocarbon migration above salt diapirs, but the strict association with the presence of oil should be considered carefully. In fact, the high amplitude bodies are typical of MDAC or gas hydrates that can also form in association with biogenic methane seepage. Assuming that anhydrite dissolution may contribute to the high amplitudes observed close to the diapir, the high amplitude might be restricted to the evaporite contexts.

Double negative polarity reflection could be a distinctive criterion for the recognition of thermogenic seep sites (***Li et al., 2015***).

The asphalt deposits are detectable from acoustic anomalies on the seafloor, which constitutes a valuable distinctive criteria. The recognition of asphalt mounds on bathymetry imagery yet requires very high-resolution data. The specific response of asphalt in sedimentary series still needs to be tested taking into account the carbonate concretions might also induce geophysical disturbances.

The active oil seep sites investigated in this study corresponds to complex seafloor features, which appear as a distinctive feature on the seafloor in the LCB. Cluster of heterometric pockmarks are characterised by an association of a great number of depressions of different sizes and asphalt mounds on the seafloor and gathers the characteristics of cluster pockmarks described by ***Andresen et al. (2012)***, who also suggested thermogenic migration from those features along salt flanks. A consortium of factors, such as the diapiric deformation, pipe locations and hydrate distribution probably controls the complexity of thermogenic pockmarks (Fig. 11). Seafloor hard-ground authigenic carbonates might also contribute to seafloor roughness (***Römer et al., 2014***). The peripheral migration of asphalt materials also amplified the seafloor roughness at the location of oil supplying seafloor seeps (Fig. 4 and Fig. 5). The proximity of the underlying salt diapir presumably enhances hydrate dissociation/dissolution over time. In the literature, pockmarks are sorted into two main categories (Type I and II; ***Riboulot et al., 2011; 2016***). Type I corresponds to "classic" conical pockmarks associated with focused fluid flow. Type II corresponds to large irregular, flat-bottomed pockmarks (~250 m in diameter) associated with the dissociation or dissolution of underlying hydrate nodules under the condition of fluid expulsion cessation or environmental changes (***Sultan et al., 2010***). The cluster of heterometric pockmarks described in this paper present geometrical similarities with the Type II pockmarks (***Riboulot et al., 2011; 2016***) that are associated with spontaneous or progressive (***Wei et al., 2015***) hydrate dissociation/dissolution. Hydrates dissociation could possibly occur in this case at the BGHSZ, the difference being that hydrate would dissociate in the context of

706 thermal anomaly instead of a seepage disruption. The complexity of seafloor seeps appear to be a
707 distinctive feature between oil/gas and water pockmarks and shall be considered for further
708 investigations in relation with peri-diapiric contexts in the LCB.

709 6. Conclusions

710 The combination of a 3D seismics with high-resolution near-surface seismic sections provided a
711 complementary and comprehensive study of the geophysical signature of an active oil seep in the
712 LCB. The recognition of recurrent oil slicks expelled from natural seafloor seeps with satellite imagery
713 demonstrated the thermogenic hydrocarbon migration. This study focuses on a large seeping zone
714 located at the rim of a salt canopy and composed of a large number of pockmarks and asphalt
715 mounds, forming a 1 km² seeping zone on the seafloor.

716 • A mini-graben, controlled by the combination of concentric conjugate faults at the diapir
717 crest, controls the location and probably the shape of the seeping zone.
718 • The oil-supplying pockmark complex is characterised by positive anomalies on backscatter
719 data and seafloor amplitudes and corresponds to seafloor high-impedance layers in the sub-
720 bottom profiler. Strong seafloor anomalies are linked to high amplitudes on exploration
721 seismics and organised as vertical pipes above the base of gas hydrate stability zone.
722 • Seafloor asphalt mound fields that develop at peripheral areas are linked by shallow faults
723 with buried HIL probably composed of restricted-size carbonate precipitations or hydrates.
724 We propose that the fluid migration is dispersed with moderate flux at the asphalt mound
725 location.
726 • The fluid bypass system at the crest of the diapir is characterised by two parallel and
727 crosscutting negative reflections. The first refers to the BGHSZ of hydrate 1 structure.
728 Assuming that the identification of recurrent oil slicks certifies thermogenic migration, the

729 second negative reflection is probably related to the stability base of hydrate structure 2
730 and/or H associated with the migration of a heavier gas mixture.

731 To conclude, this case study inventories a series of geophysical attributes associated with an active
732 thermogenic oil seep in the LCB. Among the identified anomalies, some features appear to be
733 distinctive features of thermogenic seepage, such as double BSR and rough seafloor, while the others
734 could also be associated biogenic seepage such as vertical pipes, the high impedance layer or the
735 consistent shallow high amplitudes. The geophysical anomalies inventory will be tested considering a
736 larger province and a greater oil seep site collection for relevance.

737 Acknowledgements

738 The authors express their grateful thanks to Total SA for permitting the publication of the data. This
739 study was conducted as part of a PhD project in the framework of a CIFRE contract funded by Total
740 SA in collaboration with University of Perpignan, France and granted by the ANRT (Agence Nationale
741 de la Recherche et de la Technologie), No. 2014/0308. The satellite data were provided by the
742 European Space Agency (Envisat WSM, IMP), Canadian Space Agency (Radarsat), German Aerospace
743 Centre (TerraSAR-X) and Italian Space Agency (Cosmo-Skymed). The sub-bottom profiler data were
744 provided by Total. We are grateful for the disclosure approval of Total Angola and partners. Seismic
745 interpretation was carried out using Total's proprietary software Sismage.

746 References

Abrams, M.A. (2005), Significant of hydrocarbon seepage relative to petroleum generation and entrapment, Marine and Petroleum Geology 22, p. 457-477.

Acosta, J., Uchupi, E., Muñoz, A., Herranz, P., Palomo, C., Ballesteros, M., ZEE Working Group. (2005), Salt diapirs, salt brine seeps, pockmarks and surficial sediment creep and slides in the Canary Channel off NW Africa. In Geophysics of the Canary Islands (pp. 41-57). Springer Netherlands. DOI 10.1007/s11001-004-1161-7.

Alpers, W., Espedal, H.A. (2004), Oils and Surfactants in SAR Marine User's Manual.

Andreassen, K., Mienert, J., Bryn, P., Singh, S. C. (2000), A double gas-hydrate related bottom simulating reflector at the Norwegian continental margin. Annals of

the New York Academy of Sciences, 912(1), 126-135.

Andresen, K.J. (2012), Fluid flow features in hydrocarbon plumbing systems: What do they tell us about the basin evolution, Marine Geology, 332-334, 89-108, http://dx.doi.org/10.1016/j.margeo.2012.07.006.

Andresen K.J., & Huuse, M. (2011), 'Bulls-eye' and polygonal faulting in the Lower Congo Basin: Relative timing and implications for fluid expulsion during shallow burial, Marine Geology 279, 111-127, http://dx.doi.org/10.1016/j.margeo.2010.10.016.

Andresen, K.J., Huuse, M., Shödt., N.H., Clausen, F., Seidler, L. (2011), Hydrocarbon plumbing systems of salt minibasins offshore Angola revealed by three-dimensional seismic analysis, AAPG Bulletin, 95, 1039-1065, http://dx.doi.org/10.1306/12131010046.

Anka, Z., Ondrak, R., Kowitz, A., Schodt, N. (2013), Identification and numerical modeling of hydrocarbon leakage in the Lower Congo Basin: Implications on the genesis ok km-wide seafloor mounded structures, Tectonophysics, 604, 153-171, http://dx.doi.org/10.1016/j.tecto.2012.11.020.

Anka, Z., Séranne, M., Lopez, M., Scheck-Wenderoth, M., Savoye, B. (2009), The long-term evolution of the Congo deep-sea fan: A basin-wide view of the interaction between a giant submarine fan and a mature passive margin (ZaiAngo project), Tectonophysics 470, 42-56, http://dx.doi.org/10.1016/j.tecto.2008.04.009.

Arning, E. T., Gaucher, E. C., van Berk, W., Schulz, H. M. (2015), Hydrogeochemical models locating sulfate-methane transition zone in marine sediments overlying black shales: A new tool to locate biogenic methane?. Marine and Petroleum Geology, 59, 563-574.

Bangs, N. L., Musgrave, R. J., Tréhu, A. M. (2005), Upward shifts in the southern Hydrate Ridge gas hydrate stability zone following postglacial warming, offshore Oregon. Journal of Geophysical Research: Solid Earth, 110(B3).

Beglinger, S.E., Doust, H., Cloestingh, S. (2012), Relating petroleum system and play development to basin evolution: West African South Atlantic basins, Marine and Petroleum Geology, 30, 1-25, http://dx.doi.org/10.1016/j.marpetgeo.2011.08.008.

Berger, W. H., Wefer, G., Richter, C. (1998), Color cycles in Quaternary sediments from the Congo Fan region (Site 1075): a statistical analysis. In Proceedings of the Ocean Drilling Program. Initial reports (Vol. 175, pp. 561-567). Ocean Drilling Program.

Berndt, C., Bünz, S., Clayton, T., Mienert, J., Saunders, M. (2004), Seismic character of bottom simulating reflectors: examples from the mid-Norwegian margin. Marine and Petroleum Geology, 21(6), 723-733.

Borowski, W. S., Paull, C. K., Ussler, W. (1999), Global and local variations of interstitial sulfate gradients in deep-water, continental margin sediments: Sensitivity to underlying methane and gas hydrates. Marine Geology, 159(1), 131-154.

Brekke, C., Solberg, A.H.S. (2005), Oil spill detection by satellite remote sensing, Remote Sensing of Environment, 95, 1-13,

http://dx.doi.org/10.1016/j.rse.2004.11.015.

Brice, S.E., Cochran, M.D., Pardo, G., Edwards, A.D. (1982), Tectonics and sedimentation of the South Atlantic Rift Sequence: Cabinda, Angola. American Association Petroleum Geologists Memoir, 34, 5– 18.

Brownfield, M.E., & Charpentier, R.R. (2006), Geology and total petroleum systems of the west-central coastal province (7203), west Africa (No. 2207-B).

Brun, J.P., & Fort, X. (2004), Compressional salt tectonics (Angolan Margin), Tectonophysics, 382, 129– 150, http://dx.doi.org /10.1016/j.tecto.2003.11.014.

Bünz, S., Mienert, J., Bryn, P., Berg, K. (2005), Fluid flow impact on slope failure from 3D seismic data: a case study in the Storegga Slide. Basin Research, 17(1), 109-122.

Burwood, R. (1999), Angola: source rock control for Lower Congo Coastal and Kwanza Basin petroleum systems, Geological Society, London, Special Publications v. 152, p181-184.

Cai, C., Xie, Z., Worden, R. H., Hu, G., Wang, L., & He, H. (2004), Methane-dominated thermochemical sulphate reduction in the Triassic Feixianguan Formation East Sichuan Basin, China: towards prediction of fatal H 2 S concentrations. Marine and Petroleum Geology, 21(10), 1265-1279.

Calvès, G., Huuse, M., Schwab, A., Clift, P. (2008), Three-dimensional seismic analysis of high-amplitude anomalies in the shallow subsurface of the Northern Indus Fan: Sedimentary and/or fluid origin. Journal of Geophysical Research: Solid Earth, 113(B11).

Cartwright, J., James, D., Bolton, A. (2003), The genesis of polygonal fault systems: a review. Geological Society, London, Special Publications, 216(1), 223-243.

Charlou, J.L., Donval, J.P., Fouquet, Y., Ondreas, H., Knoery, J., Cochonat, P., Levaché, D., Poirier, Y., Jean-Baptiste, P., Fourré, E., Chazallon, B. (2004), Physical and chemical characterization of gas hydrates and associated methane plumes in the Congo–Angola Basin Chemical Geology, 205, 405 – 425, http://dx.doi.org/10.1016/j.chemgeo.2003.12.033.

Chong, Z. R., Chan, A. H. M., Babu, P., Yang, M., Linga, P. (2015), Effect of NaCl on methane hydrate formation and dissociation in porous media. Journal of Natural Gas Science and Engineering, 27, 178-189.

Çifçi, G., Dondurur, D., Ergün, M. (2003), Deep and shallow structures of large pockmarks in the Turkish shelf, Eastern Black Sea. Geo-Marine Letters, 23(3-4), 311-322. DOI 10.1007/s00367-003-0138-x.

Cole, G. A., Requejo, A.G., Ormerod, D., Yu, Z., Clifford, A. (2000), Petroleum geochemical assessment of the Lower Congo Basin, in Mello, M.R., and Katz, B.J., eds., Petroleum systems of South Atlantic margins: AAPG Memoir 73, p.325-339.

Cullen, J., Mosher, D. C., Louden, K. (2008), The Mohican channel gas hydrate zone, Scotian slope: geophysical structure.

Cuss, R., Harrington, J., Giot, R., Auvray, C. (2014), Experimental observations of mechanical dilation at the onset of gas flow in Callovo-Oxfordian

claystone. Geological Society, London, Special Publications, 400(1), 507-519.

Da Costa, J.L., Schirmer, T.W., Laws, B.R. (2000), Lower Congo basin, Deepwater Exploration Province, Offshore West Africa, Second Wallace E. Pratt memorial Conference 3 Petroleum Provinces of the 21st Century.

Davies, R. J., & Cartwright, J. (2002), A fossilized Opal A to Opal C/T transformation on the northeast Atlantic margin: support for a significantly elevated Palaeogeothermal gradient during the Neogene?. Basin Research, 14(4), 467-486.

Davison, I. (1999), Tectonics and hydrocarbon distribution along the Brazilian South Atlantic margin. Geological Society, London, Special Publications, 153(1), 133-151.

De Beukelear, S.M., MacDonald, I.R., Guinasso, N.L., Murray, J.A. (2003), Distinct side-scan sonar, RADARSAT SAR, and acoustic profiler signatures of gas and oil seeps on the Gulf of Mexico slope, Geo-Marine Letters, 23, 177-186.

De Boever, E., Swennen, R., Dimitrov, L. (2006), Lower Eocene carbonate-cemented "chimney" structures (Varna, Bulgaria)—control of seepage rates on their formation and stable isotopic signature. Journal of Geochemical Exploration, 89(1), 78-82.

Dickens, G. R. (2001). Sulfate profiles and barium fronts in sediment on the Blake Ridge: present and past methane fluxes through a large gas hydrate reservoir. Geochimica et Cosmochimica Acta, 65(4), 529-543.

Dupré, S., Woodside, J., Foucher, J. P., De Lange, G., Mascle, J., Boetius, A., Harmégnies, F. (2007), Seafloor geological studies above active gas chimneys off Egypt (Central Nile Deep Sea Fan). Deep Sea Research Part I: Oceanographic Research Papers, 54(7), 1146-1172.

Duval, B., Cramez, C., Jackson, M.P.A. (1991), Raft tectonics in the Kwanza Basin, Angola, Marine and Petroleum Geology, 9, 389 – 404.

Espedal, H.A., Johannessen, O.M. (2000), Detection of oil spills near offshore installations using synthetic aperture radar (SAR), International Journal of Remote Sensing, 21:11, 2141-2144, http://dx.doi.org/10.1080/01431160050029468.

Etiope, G. (2015). Natural Gas Seepage – The Earth's Hydrocarbon Degassing.

Feng, D., Chen, D., Peckmann, J., Bohrmann, G. (2010), Authigenic carbonates from methane seeps of the northern Congo fan: microbial formation mechanism. Marine and Petroleum Geology, 27(4), 748-756.

Ferry, J. N., Babonneau, N., Mulder, T., Parize, O., & Raillard, S. (2004). Morphogenesis of Congo submarine canyon and valley: implications about the theories of the canyons formation. Geodinamica Acta, 17(4), 241-251.

Fingas, M., & Brown, C. (2014), Review of oil spill remote sensing. Marine pollution bulletin, 83(1), 9-23. http://dx.doi.org/10.1016/j.marpolbul.2014.03.059.

Floodgate, G.D., Judd, A.G., (1992), The origins of shallow gas, Continental Shelf Research, Vol 12, No 10, pp 1145 - 1156.

Fontboté, L., & Boni, M. (Eds.) (1994), Sediment-hosted Zn-Pb Ores (Vol. 10). Springer Science & Business Media.

Fort, X., Brun, J.P., Chauvel, F. (2004), Salt tectonics on the Angolan margin, synsedimentary deformation processes, AAPG Bulletin, 88:11, 1523–1544.

Foucher, J. P., Nouzé, H., Henry, P. (2002), Observation and tentative interpretation of a double BSR on the Nankai slope. Marine Geology, 187(1), 161-175.

Franceschetti, G., Iodice, A., Riccio, D., Ruello, G. Siviero, R. (2002), SAR Raw Signal Simulation of Oil Slicks in Ocean Environments, IEEE TRANSACTIONS ON GEOSCIENCE AND REMOTE SENSING, VOL. 40, NO. 9.

Fu, Y., van Berk, W., Schulz, H. M. (2016), Hydrogen sulfide formation, fate, and behavior in anhydrite-sealed carbonate gas reservoirs: A three-dimensional reactive mass transport modeling approach. AAPG Bulletin, 100(5), 843-865.

Gade, M., Alpers, W. (1998), Imaging of biogenic and anthropogenic ocean surface films by the multifrequency/ multipolarization SIR-C/X-SAR, Journal of Geophysical Research, 103, 18851-18866.

Garcia-Pineda, O., MacDonald, I., Shedd, W. (2014), Analysis of oil-volume fluxes of hydrocarbon-seep formations on the Green canyon and Mississippi canyon: A study with 3D Seismic Attributes in combination with satellite and acoustic data, SPE Reservoirs Evaluation and Engineering.

Garcia-Pineda, O., MacDonald, I., Zimmer, B., Shedd, B., Roberts, H. (2010), Remote-sensing evaluation of geophysical anomaly sites in the outer continental slope, northern Gulf of Mexico, Deep-Sea research II 57, 1859-1869, http://dx.doi.org/10.1016/j.dsr2.2010.05.005.

Garcia-Pineda, O., Zimmer, B., Howard, M., Pichel, P., Li, X., MacDonald, I.R. (2009), Using SAR images to delineate ocean oil slicks with a texture-classifying neural network algorithm (TCNNA), Canadian journal of Remote Sensing, 35, 411-421.

Gay, A., Lopez, M., Berndt, C., Séranne, M. (2007), Geological controls on focused fluid flow associated with seafloor seeps in the Lower Congo Basin, Marine Geology 244, 68 – 92, http://dx.doi.org/10.1016/j.margeo.2007.06.003.

Gay, A., Lopez, M., Cochonat, P., Levaché, D., Sermondadaz, G., Seranne, M. (2006 a), Evidences of early to late fluid migration from an upper Miocene turbiditic cannel revealed by 3D seismic coupled to geochemical sampling within seafloor pockmarks, Lower Congo Basin, Marine and Petroleum geology 23, 387-399, http://dx.doi.org/10.1016/j.marpetgeo.2006.02.004

Gay, A., Lopez, M., Cochonat, P., Séranne, M., Levaché, D., Sermondadaz, G. (2006 b), Isolated seafloor pockmarks linked to BSRs, fluid chimneys, polygonal faults and stacked Oligocene–Miocene turbiditic paleochannels in the Lower Congo Basin, Marine Geology 226, 25 – 40, http://dx.doi.org/10.1016/j.margeo.2005.09.018.

Gay, A., Lopez, M., Ondreas, H., Charlou, J.L., Sermondadaz, G., Cochonat, P. (2006 c), Seafloor facies related to upward methane flux within a Giant Pockmark of the Lower Congo basin, Marine Geology

226, 81 – 95, http://dx.doi.org/10.1016/j.margeo.2005.09.011.

Geldof, J. B., Gafeira, J., Contet, J., Marquet, S. (2014, May), GIS Analysis Of Pockmarks From 3D Seismic Exploration Surveys. In Offshore Technology Conference. Offshore Technology Conference.

Geletti, R., & Busetti, M. (2011), A double bottom simulating reflector in the western Ross Sea, Antarctica. Journal of Geophysical Research: Solid Earth, 116(B4).

Gindre-Chanu, L., Warren, J. K., Puigdefabregas, C., Sharp, I. R., Peacock, D. C., Swart, R., Henrique, L. (2015), Diagenetic evolution of Aptian evaporites in the Namibe Basin (south-west Angola). Sedimentology, 62(1), 204-233.

Guiraud, M., Buta-Neto, A., Quesne, D. (2010), Segmentation and differential post-rift uplift at the Angola margin as recorded by the transform-rifted Benguela and oblique-to-orthogonal-rifted Kwanza basins. Marine and Petroleum Geology, 27(5), 1040-1068.

Gwiazda, R., Paull, C. K., Caress, D. W., Lorenson, T., Brewer, P. G., Peltzer, E. T., Lundsten, E. (2016), Eel Canyon slump scar and associated fluid venting. In Submarine Mass Movements and their Consequences (pp. 411-418). Springer International Publishing.

Haas, A., Peckmann, J., Elvert, M., Sahling, H., & Bohrmann, G. (2010), Patterns of carbonate authigenesis at the Kouilou pockmarks on the Congo deep-sea fan. Marine Geology, 268(1), 129-136.

Hardman-Mountford, N.J., Richardson, A.J., Agenbag, J.J., Hagen, E., Nykjaer, L., Shillington, F.A., Villacastin, C. (2003), Ocean climate of the South Esat Atlantic observed from satellite data and wind models, Progress in Oceanography, 59, 181-221, http://dx.doi.org/10.1016/j.pocean.2003.10.001.

Head, I. M., Jones, D. M., Larter, S. R. (2003), Biological activity in the deep subsurface and the origin of heavy oil. Nature, 426(6964), 344-352.

Heggland, R. (2002), Seismic evidence of vertical fluid migration through faults: applications of chimney and fault detection. In Proceedings from AAPG Hedburg Conference, Vancouver.

Hill, A.J., Fish, P.R., Thomas, S. (2010), Deepwater Angola geohazard mitigation.

Ho, S., Cartwright, J.A., Imbert, P. (2012), Vertical evolution of fluid venting structures in relation to gas flux, in the Neogene, Quaternary of the Lower Congo Bain, Offshore Angola.

Holmes, M.E., Schneider, R.R., Müller, P.J. (1997), Reconstruction of past nutrient utilization in the eastern Angola Basin based on sedimentary 15N/14N ratio1997, Paleoceanography, 12:4, 604-614.

Hood, K. C., Wenger, L. M., Gross, O. P., Harrison, S. C. (2002), Hydrocarbon systems analysis of the northern Gulf of Mexico: Delineation of hydrocarbon migration pathways using seeps and seismic imaging, in Surface exploration case histories: Applications of geochemistry, magnetics, and remote sensing, D. Schumacher and L. A. LeSchack, eds., AAPG Studies in Geology No. 48 and SEG Geophysical References Series No. 11, p. 25–40.

Hopkins, J., Lucas, M., Dufau, C., Sutton, M., Stum, J. (2013), Detection and variability of the Congo River plume from satellite derived sea surface temperature, salinity, ocean colour and sea level. Remote Sensing of Environment, 139, 365-385.

Hovland, M. (1981), A classification of pockmark related features in the Norwegian Trench. IKU, Institutt for Kontinentalsokkelundersøkelser.

Hovland, M., Heggland, R., De Vries, M.H., Tjelta, T.I. (2010), Unit-pockmarks and their potential significance for predicting fluid flow, Marine and Petroleum Geology 27, 1190 – 1199, doi:10.1016/j.marpetgeo.2010.02.005.

Hovland., M., & Irwin., H. (1992), Habitat of Methanogenic Carbonate cemented sediments in the North Sea, Bacterial Gas, 157 – 172.

Hovland, M., & Judd, A. G. (1988), Seabed pockmarks and seepages: Impact on geology, biology and the marine environment: London. Graham and Trotman, 293p.

Hovland, M., Judd, A. G., King, L. H. (1984), Characteristic features of pockmarks on the North Sea Floor and Scotian Shelf. Sedimentology, 31(4), 471-480.

Hovland, M., Svensen, H. (2006), Submarine pingoes: Indicators of shallow gas hydrates in a pockmark at Nyegga, Norwegian Sea, Marine Geology 228, pp.15–23.

Hovland, M., Talbot, M.R., Qvale, H., Olaussen, S., Assberg, L. (1987), Methane-related carbonate cements in pockmarks of the North Sea, Journal of Sedimentary Petrology, 57:5, 881 - 892.

Huuse, J. D., Palmer, C., Cole, V. (2014, June), Deepwater Papua New Guinea-Evidence for a Working Petroleum System. In 76th EAGE Conference and Exhibition 2014.

Imbert, P., & Ho, S. (2012). Seismic-scale funnel-shaped collapse features from the Paleocene–Eocene of the North West Shelf of Australia. Marine Geology, 332, 198-221.

Ivanov, M. V., Lein, A. Y., Reeburgh, M. S., Skyring, G.W. (1989), Interaction of sulphur and carbon cycles in marine sediments. Evolution of the Global Biogeochemical Sulphur Cycle. Wiley, Chichester, 125-79.

Jackson, C. A. L., & Lewis, M. M. (2012), Origin of an anhydrite sheath encircling a salt diapir and implications for the seismic imaging of steep-sided salt structures, Egersund Basin, Northern North Sea. Journal of the Geological Society, 169(5), 593-599.

Jansen, J. H. F. (1985). Hiatuses in Mesozoic and Cenozoic sediments of the Zaire (Congo) continental shelf, slope, and deep-sea fan. South Atlantic Paleoceanography (Eds KJ Hsu and HJ Weissert), 197-204.

Jatiault, R., Dhont, D., Loncke, L., Dubucq, D. (2017), Monitoring of natural oil seepage in the Lower Congo Basin using SAR observations. Remote Sensing of Environment, 191, 258 - 272. http://dx.doi.org/10.1016/j.rse.2017.01.031.

Jatiault, R., Dhont, D., Loncke, L., Durrieu de Madron, X., Dubucq, D., Channeliere, C., & Bourrin, F. (2018). Behavior of natural oil droplets through the water column in deep-water environments: The case of the Lower Congo Basin. Submitted to Deep Sea Research Part I.

Johannessen., O. M., Sandven, M., Jenkins, A. D., Durand, D., Petterson, L. H., Espedal, H., Evensen, G., Hamre, T. (2000), Satellite earth observation in operational oceanography, Coastal Engineering, 41, 155-176.

Jones, D.O.B. Walls, A., Clare, M., Fiske, M.S.,Weiland, R.J., O'Brien, R., Touzel, D.F. (2014), Asphalt mounds and associated biota on the Angolan margin, Deep-Sea Research I, http://dx.doi.org/10.1016/j.dsr.2014.08.010.

Judd, A., & Hovland, M. (2009), Seabed fluid flow: the impact on geology, biology and the marine environment. Cambridge University Press.

Karner, G. D., Driscoll, N. W., McGinnis, J. P., Brumbaugh, W. D., Cameron, N. R. (1997), Tectonic significance of syn-rift sediment packages across the Gabon-Cabinda continental margin. Marine and Petroleum Geology, 14(7-8), 973-1000.

Karstens, J., & Berndt, C. (2015), Seismic chimneys in the Southern Viking Graben–Implications for palaeo fluid migration and overpressure evolution. Earth and Planetary Science Letters, 412, 88-100.

Keller, E. A., Duffy, M., Kennett, J. P., & Hill, T. (2007), Tectonic geomorphology and hydrocarbon induced topography of the mid-channel Anticline, Santa Barbara Basin, California. Geomorphology, 89(3), 274-286.

King, L.H., & MacLean, B. (1970), Pockmark on the Scotian Shelf, Geological Society of America Bulletin, V.81, P.3141-3148.

Korber, J.H., Sahling, H., Pape, T., dos Santos Fereira, C., MacDonald, I., Bohrmann, G. (2014), Natural oil seepage at Kobuleti Ridge, eastern Black Sea. Marine and Petroleum Geology, 50, 68- 82, http://dx.doi.org/10.1016/j.marpetgeo.2013.11.007.

Kornacki, A.S., Kendrick, J.W., Berry, J.L. (1994), Impact of oil and gas vents and slicks on petroleum exploration in the deepwater Gulf of Mexico, Geo-Marine Letters, 14, 160-169.

Kvenvolden K.A., & Cooper C.K. (2003). Natural seepage of crude oil into the marine environment, Geo-Marine Letters, 23, 140-146, http://dx.doi.org/10.1007/s00367-003-0135-0.

Kvenvolden, K.A., & Harbaugh, J.W. (1983). "Reassessment of the Rates at which Oil from Natural Sources Enters the Marine Environment". USGS Staff -- Published Research. Paper 426. http://digitalcommons.unl.edu/usgsstaffpub/426.

Larter, S., Huang, H., Adams, J., Bennett, B., Jokanola, O., Oldenburg, T., Fowler, M. (2006), The controls on the composition of biodegraded oils in the deep subsurface: Part II—Geological controls on subsurface biodegradation fluxes and constraints on reservoir-fluid property prediction1. AAPG bulletin, 90(6), 921-938.

Larter, S., Wilhelms, A., Head, I., Koopmans, M., Aplin, A., Di Primio, R., Telnaes, N. (2003), The controls on the composition of biodegraded oils in the deep subsurface—part 1: biodegradation rates in petroleum reservoirs. Organic Geochemistry, 34(4), 601-613.

Lee, G. H., Kim, H. J., Jou, H. T., Cho, H. M. (2003), Opal-A/opal-CT phase boundary inferred from bottom-simulating

reflectors in the southern South Korea Plateau, East Sea (Sea of Japan). Geophysical research letters, 30(24).

Lehner, P., & De Ruiter, P. A. C. (1977), Structural history of Atlantic margin of Africa. AAPG Bulletin, 61(7), 961-981.

León, R., Somoza, L., Medialdea, T., Maestro, A., Díaz-del-Río, V., del Carmen Fernández-Puga, M. (2006), Classification of sea-floor features associated with methane seeps along the Gulf of Cádiz continental margin. Deep Sea Research Part II: Topical Studies in Oceanography, 53(11), 1464-1481.

Li, L., Liu, H., Zhang, X., Lei, X., Sha, Z. (2015), BSRs, estimated heat flow, hydrate-related gas volume and their implications for methane seepage and gas hydrate in the Dongsha region, northern South China Sea. Marine and Petroleum Geology, 67, 785-794.

Lobo, F. J., & Ridente, D. (2013), Milankovitch cyclicity in modern continental margins: stratigraphic cycles in terrigenous shelf settings. Boletín Geológico y. Minero, 124(2), 169-185.

Loncke, L., Mascle, J., Fanil Scientific Parties (2004), Mud volcanoes, gas chimneys, pockmarks and mounds in the Nile deep-sea fan (Eastern Mediterranean): geophysical evidences. Marine and Petroleum Geology, 21, pp 669 – 689, doi:10.1016/j.marpetgeo.2004.02.004.

Løseth, H., Wensaas, L., Arntsen, B., Hanken, N. M., Basire, C., Graue, K. (2011), 1000 m long gas blow-out pipes. Marine and Petroleum Geology, 28(5), 1047-1060.

Lucazeau, F., Brigaud, F., Bouroullec, J. L. (2004), High-resolution heat flow density in the lower Congo basin, Geochemistry, Geophysics, Geosystems, 5, http://dx.doi.org/10.1029/2003GC000644 .

MacDonald, I. R., Bohrmann, G., Escobar, E., Abegg, F., Blanchon, P., Blinova, V., Heeschen, K. (2004), Asphalt volcanism and chemosynthetic life in the Campeche Knolls, Gulf of Mexico. Science, 304(5673), 999-1002.

Macdonald, I.R., Guinasso, N.L., Ackleson, S.G., Amos, J.F., Duckworth, R., Sassen, R. (1993), Natural oil slicks in the gulf of Mexico visible from space, Journal of Geophysical Research, 98, 16351 – 16364.

Macdonald, I.R., Leifer, I., Sassen, R., Stine, P., Mitchell, R., Guinasso, J.N. (2002), Transfer of hydrocarbons from natural seeps to the water column and atmosphere. Geofluids, 2, 95-107.

MacDonald, I. R., J. F. Reilly, Jr., S. E. Best, R. Venkataramaiah, R. Sassen, N. L. Guinasso, Jr., Amos, J. (1996), Remote sensing inventory of active oil seeps and chemosynthetic communities in the northern Gulf of Mexico, in D. Schumacher and M. A. Abrams, eds., Hydrocarbon migration and its near-surface expression: AAPG Memoir, 66, 27–37.

MacHargue, T.R. (1990), Stratigraphic Development of Proto-South Atlantic Rifting in Cabinda, Angola - A Petroliferous Lake Basin. In Katz, B.J. (Ed.) Lacustrine Basin Exploration Case Studies and Modern Analogs, 50. AAPG Memoir, p.307-326.

Machel, H. G. (2001), Bacterial and thermochemical sulfate reduction in diagenetic settings—old and new

insights. Sedimentary Geology, 140(1), 143-175.

Macmahon, J., Pecher, I., Crutchley, G., Mountjoy, J., Krastel, S., Henrys, S. (2014), QUANTITATIVE SEISMIC ANALYSIS OF DOUBLE-BSRs ON THE HIKURANGI MARGIN.

Maia, A. R., Cartwright, J., Andersen, E. (2016), Shallow plumbing systems inferred from spatial analysis of pockmark arrays. Marine and Petroleum Geology, 77, 865-881.

Marcon, Y., Ondréas, H., Sahling, H., Bohrmann, G., Olu, K., (2014), Fluid flood regimes and growth of a giant pockmark, Geology, Vol.42, Issue 1, pp.63 – 66. http://dx.doi.org/10.1130/G34801.1.

Marton, G., Carpenter, D., Greg, S. (2004), Salt Tectonics of the Continent-Ocean Transition, Deep-Water Angola: Concepts, Applications and Case Studies for the 21st Century, 24th Annual GCSSEPM Foundation Bob F. Perkins Research Conference pp.709 – 735.

Marton, G.L., Tari, G. C., Lehmann, C. T. (2000), Evolution of the Angolan Passive Margin, West Africa, With Emphasis on Post-Salt Structural Styles. Atlantic rifts and continental margins, 129-149.

McCandless, S.W., & Jackson, C.R. (2003), Principles of Synthetic Aperture Radar in Synthetic Aperture Radar Marine User's Manual, 1-24.

McKelvey, V. E. (1986), Subsea mineral resources (No. 1689). Dept. of the Interior, US Geological Survey.

Moss, J. L., & Cartwright, J. (2010), 3D seismic expression of km scale fluid escape pipes from offshore Namibia. Basin Research, 22(4), 481-501.

Moulin, M., Aslanian, D., Olivet, J. L., Contrucci, I., Matias, L., Géli, L., Unternehr, P. (2005), Geological constraints on the evolution of the Angolan margin based on reflection and refraction seismic data (ZaïAngo project). Geophysical Journal International, 162(3), 793-810.

Moulin, M., Aslanian, D., Unternehr, P. (2010), A new starting point for the South and Equatorial Atlantic Ocean. Earth-Science Reviews, 98(1), 1-37.

Nyamapfumba, M., & McMechan, G. A. (2012), Gas hydrate and free gas petroleum system in 3D seismic data, offshore Angola. Geophysics, 77(6), O55-O63.

Nyman, S. L., Nelson, C. S., Campbell, K. A., Schellenberg, F., Pearson, M. J., Kamp, P. J., King, P. R. (2006), Tubular carbonate concretions as hydrocarbon migration pathways? Examples from North Island, New Zealand.

National Research Council Committee on Oil in the Sea, (2003). Oil in the Sea III: Inputs, Fates and Effects. (280 pp.). The National Academies Press, Washington, D. C.

Ondreas, H., Olu, K., Fouquet, Y., Charlou, J.L., Gay, A., Dennielou, B., Donval, J.P., Fifis, A., Nadalig, T., Cochonat, P., Cauquil, E., Bourillet, J.F., Le Moigne, M., Sibuet, M. (2005), ROV study of a giant pockmark on the Gabon continental margin, Geo-Marine Letters, 25, 281-292, http://dx.doi.org/10.1007/s00367-005-0213-6.

Oluboyo, A.P., Gawthorpe, R.L., Bakke, K., Hadler-Jacobsen, F. (2014), Salt tectonic controls on deep-water turbidite depositional systems: Miocene,

southwestern Lower Congo Basin, offshore Angola, Basin Research 26, 597–620, doi: 10.1111/bre.12051.

Paull, C. K., & Ussler, W. (2008), Re-evaluating the significance of seafloor accumulations of methane-derived carbonates: seepage or erosion indicators?.

Pecher, I., Crutchley, G., Mountjoy, J., Gorman, J., Fraser, D., Kroeger, K., Henrys, S. (2014), Double-BSRs on the Hikurangi Margin: Link Between Gas Hydrates and Conventional Petroleum System?

Peters, K.E., Walters, C.C., Moldowan, J.M. (2007), The Biomarker Guide Volume 2, Biomarkers and Isotopes in Petroleum Systems and Earth History.

Petersen, C. J., Bünz, S., Hustoft, S., Mienert, J., Klaeschen, D. (2010), High-resolution P-Cable 3D seismic imaging of gas chimney structures in gas hydrated sediments of an Arctic sediment drift. Marine and Petroleum Geology, 27(9), 1981-1994.

Peterson, R.G., Stramma, L. (1991), Upper-level circulation in the South Atlantic Ocean, Progress in Oceanography, 26, 1-73.

Pierre, C., & Fouquet, Y. (2007), Authigenic carbonates from methane seeps of the Congo deep-sea fan. Geo-Marine Letters, 27(2-4), 249-257.

Popescu, I., Lericolais, G., Panin, N., De Batist, M., Gillet, H. (2007), Seismic expression of gas and gas hydrates across the western Black Sea. Geo-Marine Letters, 27(2-4), 173-183.

Posewang, J., & Mienert, J. (1999), The enigma of double BSRs: indicators for changes in the hydrate stability field?. Geo-Marine Letters, 19(1-2), 157-163.

Posey, H. H., Kyle, J. R., Jackson, T. J., Hurst, S. D., & Price, P. E. (1987). Multiple fluid components of salt diapirs and salt dome cap rocks, Gulf Coast, USA. Applied geochemistry, 2(5-6), 523-534.

Qi, Y., Wu, W., Liu, Y., Xie, Y., Chen, X. (2012), The influence of NaCl ions on hydrate structure and thermodynamic equilibrium conditions of gas hydrates. Fluid Phase Equilibria, 325, 6-10.

Riboulot, V. (2011), Facteurs de contrôle du fonctionnement des pockmarks durant les derniers cycles climatiques, Partie orientale du delta sous-marin du Niger et Golfe du Lion. Université de Perpignan Via Domitia, Ecole Doctorale Energie Environnement, 243p.

Riboulot, V., Sultan, N., Imbert, P., Ker, S. (2016), Initiation of gas-hydrate pockmark in deep-water Nigeria: Geo-mechanical analysis and modelling. Earth And Planetary Science Letters, 434, 252-263.

Roberts, H.H., Hardage, B.A., Shedd, W.W. (2006), Seafloor reflectivity - An important seismic property for interpreting fluid/gas expulsion geology and the presence of gas hydrate. The Leading Edge, pp.620 – 628.

Römer, M., Sahling, H., Pape, T., dos Santos Ferreira, C., Wenzhöfer, F., Boetius, A., &

Sahling, H., Blum, M. R., Borowski, C., Escobar-Briones, E., Gaytán-Caballero, A., Hsu, C. W., Römer, M. (2016), Seafloor observations at Campeche Knolls, southern Gulf of Mexico: coexistence of asphalt deposits, oil seepage, and gas venting.

Sassen, R., Cole, G. A., Drozd, R., Roberts, H. H. (1994). Oligocene to Holocene

hydrocarbon migration and salt-dome carbonates, northern Gulf of Mexico. Marine and Petroleum Geology, 11(1), 55-65.

Savoye, B., Babonneau, N., Dennielou, B., & Bez, M. (2009). Geological overview of the Angola–Congo margin, the Congo deep-sea fan and its submarine valleys. Deep Sea Research Part II: Topical Studies in Oceanography, 56(23), 2169-2182.

Schneider, R.R., Müller, P.J., Ruhland, G., Meinecke, G., Schmidt, H., Wefer, G. (1996), Late Quaternary Surface Temperatures and Productivity in the East-Equatorial South Atlantic: Response to Changes in Trade/ Monsoon Wind Forcing and Surface Water Advection in Wefer, G., Berger, W.H., Siedler, G., Webb, O.J., 1996, The South Atlantic: Present and Past Circulation, 527 – 551.

Schoellkopf, N. B., Patterson, B.A. (2000), Petroleum systems of offshore, Cabinda, Angola, in M. R. Mello and B. J. Katz, Petroleum systems of South Atlantic margins: AAPG Memoir 73, 361–376.

Seewald, J. S. (2003), Organic–inorganic interactions in petroleum-producing sedimentary basins. Nature, 426(6964), 327-333.

Séranne, M., & Anka, Z. (2005), South Atlantic continental margins of Africa: a comparison of the tectonic vs climate interplay on the evolution of equatorial west Africa and SW Africa margins. Journal of African Earth Sciences, 43(1), 283-300.

Serié, C., Huuse, M., Schødt, N. H., Brooks, J. M., & Williams, A. (2016), Subsurface fluid flow in the deep-water Kwanza Basin, offshore Angola. Basin Research.

Shannon., L.V. (2001), Benguela Current, in Ocean Currents: a derivative of encyclopedia of Ocean Sciences, 2nd Edition, p. 23-34.

Sloan, E. D. (1990), Clathrate Hydrates of Natural Gases, 1st ed., 641 pp., Marcel Dekker, New York.

Sloan, E. D. (2003), Fundamental principles and applications of natural gas hydrates. Nature, 426(6964), pp 353-363.

Stafford, K. W., Ulmer-Scholle, D., Rosales-Lagarde, L. (2008), Hypogene calcitization: Evaporite diagenesis in the western Delaware Basin. Carbonates and evaporites, 23(2), 89.

Stolper, D.A., Martini, A.M., Clog, M., Douglas, P.M., Shusta, S.S., Valentine, D.L., Sessions, A.L., Eiler, J.M., Distinguishing and understanding thermogenic and biogenic sources of methane using multiply substituted isotopologues, Geochimica et Cosmochimica Acta (2015), doi: http://dx.doi.org/10.1016/j.gca. 2015.04.015.

Stramma, L., & England M. (1999), On the water masses and mean circulation of the South Atlantic Ocean, Journal of Geophysical research, 104, 20863 – 20883.

Sultan, N., Marsset, B., Ker, S., Marsset, T., Voisset, M., Vernant, A. M., Drapeau, D. (2010), Hydrate dissolution as a potential mechanism for pockmark formation in the Niger delta. Journal of Geophysical Research: Solid Earth, 115(B8).

Teisserenc, P., & Villemin, J. (1989), Sedimentary basin of Gabon--geology and oil systems.

Thomas, S., Hill, A. J., Clare, M. A., Shreeve, J. W., Unterseh, S. (2011, January), Understanding Engineering Challenges Posed by Natural Hydrocarbon Infiltration and the Development of Authigenic Carbonate. In Offshore Technology Conference. Offshore Technology Conference.

Uchupi, E. (1992), Angola Basin: geohistory and construction of the continental rise. Geologic Evolution of Atlantic Continental Rifts. Nostrand Reinhold, New York, 77-99.

Uenzelmann-Neben, G. (1998), Neogene sedimentation history of the Congo Fan. Marine and Petroleum Geology, 15(7), 635-650.

Unterseh, S. (2013), Early Recognition of Seabed and Sub-Seabed Natural Hydrocarbon Seeps in Deep Offshore Angola. 2013 Offshore Technology Conference, May 06 - 09, 2013, Houston, TX, USA.

Valentine, D. L., Reddy, C. M., Farwell, C., Hill, T. M., Pizarro, O., Yoerger, D. R., Clarke, B. A. (2010), Asphalt volcanoes as a potential source of methane to late Pleistocene coastal waters. Nature Geoscience, 3(5), 345-348.

Warren, J. K. (2000), Evaporites, brines and base metals: low-temperature ore emplacement controlled by evaporite diagenesis. Australian Journal of Earth Sciences, 47(2), 179-208.

Warren, J. K. (2016), Evaporites: A geological compendium. Springer.

Wei, J., Pape, T., Sultan, N., Colliat, J. L., Himmler, T., Ruffine, L.,Peters, C. A. (2015), Gas hydrate distributions in sediments of pockmarks from the Nigerian margin–Results and interpretation from shallow drilling. Marine and Petroleum Geology, 59, 359-370.

Wenau, S., Spiess, V., Pape, T., Fekete, N. (2014 a), Cold seeps at the salt front in the Lower Congo Basin I: Current methane accumulation and active seepage, Marine and Petroleum Geology, doi: 10.1016/j.marpetgeo.2014.07.032.

Wenau, S., Spiess, V., Pape, T., fekete, N. (2014 b), Cold seeps at the salt front in the Lower Congo Basin II: The impact of spatial and temporal evolution of salt-tectonics on hydrocarbon seepage, Marine and Petroleum Geology pp.1 – 14, http://dx.doi.org/10.1016/j.marpetgeo.2014.09.021

Williams, A. & Lawrence, G. (2002), The Role of Satellite Seep Detection in exploring the South Atlantic's Ultradeep Water, in Surface exploration case histories: Applications of geochemistry, magnetic, and remote sensing, , Shumacher, D., & LeSchack, L.A., eds., AAPG Studies in geology No. 48 and SEG Geophysical References Series No. 11, 327-344.

Wilson, R. D., Monaghan, P.H., Osanik, A., Price, L., C., & Rogers, M. A. (1973). Estimate of Annual input of Petroleum to the Marine Environment from Natural Marine Seepage. Trans. Gulf Coast Assoc. Geological Societies, 23, 182-193.

Zatyagalova, V.V., Ivanov, A.Y., Gobulov, B.N. (2007), Application of Envisat SAR imagery for mapping and estimation of natural oil seeps in the South Caspian Sea. In Proceedings of the Envisat Symposium 2007, 23 – 27.

Zühlsdorff, L., & Spiess, V. (2005), Three-dimensional seismic and acoustic imaging

of gas migration and gas hydrate accumulation beneath pockmarks in hemipelagic sediments off Congo, south-west Africa. In International conference on gas hydrates, Trondheim, Norway (Vol. 5).